Iron isotope and trace metal compositions of manganese nodules from the Central Indian Basin: Evidence for Fe fluxes from both hydrogenetic and oxic diagenetic sources

Bulusu Sreenivas[1, *], B. Nagender Nath[2], Y.J. Bhaskar Rao[1], B. Vijaya Gopal[1], T.C. Vineesh[2], E.V.S.S.K. Babu[1]

[1]CSIR-National Geophysical Research Institute, Hyderabad 500007, India
[2]CSIR-National Institute of Oceanography, Dona Paula, Goa 403004, India

* Corresponding Author: bsreenivas@ngri.res.in
Telephone: +91-40-27012579
Fax: +91-40-23434651

Abstract

Iron isotope compositions ($\delta^{56}Fe$) of ferromanganese (Fe-Mn) crusts and nodules are reliable proxies for understanding the biogeochemical cycling of Fe in the ocean. Fe-Mn nodules/crusts are characterized by low $\delta^{56}Fe$ values (–0.8 to –0.05 ‰ IRMM 014), while the dissolved Fe in the deep ocean is ^{56}Fe enriched ($d^{56}Fe$ range from +0.2 to +0.8 ‰). Here, we report Fe isotope compositions of top scrapings of sixteen Mn nodules and three Fe-Mn crusts and their geochemical compositions from the Central Indian Basin (CIB) to understand Fe isotope compositions. Based on their morphology and elemental compositions, the CIB nodules are divided into three groups: 'hyrogenetic,' 'diagenetic,' and 'mixed' types. The range of $\delta^{56}Fe$ values (-0.63 to -0.06 ‰) for CIB nodules and crusts is similar to those from different parts of the world ocean. The $\delta^{56}Fe$ values of the hydrogenetic group of CIB nodules are consistent with a fractionation model involving selective adsorption ^{56}Fe onto organic ligands (siderophore complexes). Using a fractionation factor of -0.77 ‰ between seawater and nodules, we estimate that $\delta^{56}Fe$ of the CIB deep seawater dissolved Fe range between +0.28 and +0.63 ‰ similar to the Atlantic deep seawater. The $\delta^{56}Fe$ values of mixed nodules correlate positively with Mn/Fe and concentrations of Mn, Cu, Zn, Mo, Cd, Sb, and Tl, and negatively with Fe, Be, Sc, Co, Zr, Nb, and rare earth elements (REE). These mixing lines attest to variable proportions of metals from diagenetic and hydrogenetic sources.

Keywords: Fe isotope compositions, Manganese nodules, Ferromanganese crusts, Central Indian Basin, Trace and REE geochemistry, Isotope fractionation

1 INTRODUCTION

The biogeochemical cycling of Fe in the global ocean has received considerable attention because of its role as a limiting nutrient controlling the primary productivity in the surface ocean (Martin et al., 1990). Fe isotope compositions of ferromanganese nodules and encrustations form an essential source of information for the Fe cycling in the ocean on time scales of millions of years (Zhu et al., 2000; Levasseur et al., 2004; Chu et al., 2006, Horner et al., 2015; Marcus et al., 2015). Temporal variations in δ^{56}Fe of Fe-Mn crusts from Atlantic were the focus of initial studies suggesting a linkage between Fe isotope compositions and terrestrial Fe input into the ocean (Zhu et al., 2000). Levasseur et al. (2004) analyzed spatial variations in δ^{56}Fe of Fe-Mn crusts on a global scale concluding that local-scale processes are significant in influencing the Fe isotope variations. The Fe isotope compositions of Pacific crusts revealed complex hydrothermal fluid mobility pathways in oceanic environments (Chu et al., 2006). The ferromanganese crusts and nodules analyzed from different parts of the world ocean exhibit δ^{56}Fe values ranging between –0.8 and –0.05 ‰ IRMM-014 (Levasseur et al., 2004), distinctly depleted in ^{56}Fe relative to the average crustal Fe with δ^{56}Fe of 0 ‰ (Dauphas & Rouxel, 2006). Recent studies on Fe-Mn crusts from the Pacific Ocean led to identifying deeply sourced Fe (Horner et al., 2015) and eolian sources as major input (Marcus et al., 2015). Considering that the continental source contributes a much larger part of Fe flux into the ocean relative to the hydrothermal influx, these ^{56}Fe-depleted values remain enigmatic (Beard et al., 2003a). Highly negative δ^{56}Fe values are reported for diagenetic pore fluids especially in shallow water environments (Bergquist & Boyle, 2006; Severmann et al., 2006; 2008) and coastal settings (Rouxel et al., 2008a), suggesting that diagenesis could have played a significant role in ^{56}Fe depletion in nodules and crusts. However, deep

water pore fluids from the Crozet region showing δ^{56}Fe values 0 ‰ contradict this (Homoky et al., 2009). The reasons for such depletion in ^{56}Fe in crusts and nodules have therefore remain equivocal (Zhu et al., 2000; Levasseur et al., 2004; Chu et al., 2006; Anbar & Rouxel, 2007).

The majority of Fe isotope studies have focused mainly on ferromanganese crusts, while only a few manganese nodules have been analyzed. The significance of Fe isotope compositions of manganese nodules in terms of their slow growth rates, wide distribution, and Fe biogeochemical cycling remain therefore inadequately addressed. The Mn nodules occur in all the major oceanic basins, and unlike Fe-Mn crusts, the nodules form under slow sedimentation rates (< 5 mm/Ka) largely controlled by bottom water flows (Glasby, 2006). As a result, they tend to preserve regional patterns in their compositional variation despite the known micro lamina- to regional-scale disparities (von Stackelberg & Marchig, 1987), making them an excellent target to address basin-scale Fe biogeochemical processes. The Central Indian Basin is the second richest Mn nodule field (Mukhopadhyay et al., 2002) after the equatorial part of the Circum Pacific Belt (Glasby, 2006). Previous studies on the CIB nodules emphasized their continuous accretion since the Late Miocene and observed a linkage between the morphology, compositions, and spatial distribution with sedimentary and geodynamic evolution of the basin (Martin-Barajas et al., 1991; Mukhopadhyay et al., 2002). In this study, we report for the first time Fe isotope compositions of the CIB nodules alongside major, trace, REE geochemistry for the top scrapings of 16 manganese nodules and three bulk samples of ferromanganese crusts from the CIB. We suggest that the observed δ^{56}Fe variations in Mn nodules are consistent with eolian source as major Fe input and subsequent Fe isotope

fractionation associated with adsorption of heavy Fe isotope onto organic ligands. We also show that the diagenetic source of Fe played a significant role in the CIB.

2 SAMPLES AND ANALYTICAL METHODS

2.1 The Central Indian Basin nodule field

The CIB (Fig. 1a) constitutes the largest sedimentary basin (~5.7 million Km^2) in the Indian Ocean with an average water depth of ~5000 m. The Chagos-Laccadive Ridge binds the basin to the west, the Ninetyeast Ridge to the east, and the Southeast Indian Ridge in the north (not shown). The ocean floor of the CIB is formed during the Paleocene, between 60 and 49 Ma, as indicated by magnetic anomalies (Royer et al., 1989; Mukhopadhyay et al., 1997). The central parts of the CIB comprise siliceous clay and ooze, while terrigenous and pelagic clays dominate in the northern and southern parts (Fig. 1b; see Nath et al., 1989; 1992a). Parameters that control the deposition of these sediments are: (a) the equatorial productivity belt, (b) the terrigenous input and, (c) the water depth of deposition. It is estimated that the siliceous sediments in the northern part (8-10° S) were deposited during Late Miocene/Early Pliocene, while those in the southern part accumulated in the Late Pliocene (Pimm, 1971). Manganese nodules are ubiquitous throughout the CIB, reflecting generally slow sedimentation rates in the basin (Mukhopadhyay et al., 2008). They are brown to black with variable morphology and located mainly towards the south of lat. 10° S. The CIB nodules are polymetallic, and a conservative estimate suggests a reserve of 779 million metric tons of metals including Fe, Mn, Ni, Co, etc. (Mukhopadhyay et al., 2008). Three genetic types, viz. a) hydrogenetic, b) diagenetic, and c) mixed-mode nodules, were described earlier from the CIB (Martin-Barajas et al., 1991). The hydrogenetic nodules are botryoidal with a smooth surface. These are

formed by dense layers of δMnO_2–$Fe(OH)_3$ and amorphous silica. The diagenetic nodules show a granular texture and comprise concentric layers with dendritic or columnar structures, mainly of 10 Å manganate. The mixed-mode nodules show a gradation from hydrogenetic internal layers to a diagenetic outer crust. The diagenetic enrichment of metals, particularly in the upper 40 cms of siliceous sediments (< 0.4 Ma), is reflected in the presence of buserite, todorokite, and the Cu>Ni feature of the diagenetic nodules.

The density of the CIB nodules varies between 1.8 and 2.4 g/cc, with diameter commonly ranging from 20 to 60 mm (Vineesh et al., 2009). Smaller nodules are spheroid to sub-spheroid, while larger nodules are elongated, discoid, flattened, or irregular. The nuclei of CIB nodules generally comprise detrital quartz grains and clays related possibly to altered volcanic rock fragments. Broadly, nodules from the topographic highs are smooth, while those from plains have a rough morphology (Mukhopadhyay & Nath, 1988). The nodule density is highest in high productivity zones, the central zone dominated by bio siliceous oozes and sediments (Fig. 1b). In this region, the presence of todorokite [$(Na,Ca,K,Ba,Sr)_{1-x}(Mn,Mg,Al)_6O_{12} \cdot 3\text{-}4H_2O$] in the hydrogenetic nodules indicates sub-oxic conditions in the overlying water column due to the role of high primary productivity.

A slower growth rate of 1.2 to 1.3 mm/Ma for the top layers and slightly faster rates of 1.9 to 3.2 mm/Ma for the bottom ones were estimated for the CIB nodules based on the $^{230}Th_{excess}$ technique (Banakar & Borole, 1991). These growth rates translate to a Late Miocene – Early Pliocene (8 to 3 Ma) period for nodule accumulation consistent with the age of deposition of the siliceous sediments as stated above.

2.2 Sampling and sample preparation

Samples analyzed in the present study were collected during various cruises of the CSIR-National Institute of Oceanography, Goa, India, since 1982. Individual nodule samples exposing well-preserved surfaces were isolated from extensive collections. These were subjected to desalination and extended cleaning routines in deionized water. A total of 16 manganese nodule samples were randomly chosen to represent a wide geographic area in the CIB (Fig. 1a, b). Apart from the nodules, three Fe-Mn crust samples were also studied. These include a sample each from the CIB (sample# SKC), the Afanasiy-Nikitin seamount (sample# AND), and the Central Indian Ridge (sample# CIB) (Fig. 1b). Sample locations and the morphological features of nodules are summarized in Supporting Information 1. In this study, most of the nodules are recovered from the siliceous clay domain, while a few are from pelagic red clay (Fig. 1b). For analysis, the top layers of the nodules were scraped up to about 0.5 mm thickness using Teflon coated knife, and fine powders were prepared in an agate mortar. Analyses were carried out on these powders after leaching, as described in the following section. Although the exact age of accumulation of nodule top layers studied here is unknown, we presume a temporal correlation among the analyzed samples representing a recent phase of oxide accumulation. Considering growth rates of 1.2 to 1.3 mm/Ma for the top layers, the depositional age is constrained between ~600 and 650-kilo years.

2.3 Fe isotope analysis

Fe isotope analysis was carried out using the Multi-Collector Inductively Coupled Plasma Mass Spectrometer (MC-ICP-MS, model Nu Plasma HR) at CSIR-NGRI. A detailed account of the analytical protocols and performance is presented in Supporting Information 2 and described briefly below.

Mn-nodule and ferromanganese crust samples and the standards were dissolved in cold 6 N HCl followed by ultrasonication. The silicate standard BCR-2 was dissolved using concentrated $HF+HNO_3+HClO_4$. The final sample/standard solutions were taken in 7 N HCl + 0.001% H_2O_2. Elution of Fe was carried out following the procedures described in Marèchal et al. (1999). The macroporous resin AG MP-1 (100–200 mesh, chloride of BIO-RAD^{TM}) was used to separate Fe, Cu, and Zn. The eluted fractions were evaporated and re-dissolved in 2 % HNO_3 for MC-ICP-MS analysis. Iron recovery was estimated using the BCR-2 elution in each ml fraction using AAS. The Fe yields were ≥97 % based on recovery for standards indicating that fractionation during anion exchange (Anbar et al., 2000) was negligible.

The Nu HR MC-ICP-MS features a double-focusing Nier Johnson design and variable dispersion achieved by electrostatic zoom lens mechanism. A mass resolution of >5000 was achieved Using the pseudo-high resolution mode. All the Fe isotope measurements were carried out in static-multi-collector mode. Three isotopes of Fe (^{54}Fe, ^{56}Fe, and ^{57}Fe) along with ^{53}Cr were measured repeatedly.

Analysis of samples was carried out in standard-sample bracketing (SSB) mode to correct the instrumental mass fractionation using IRMM-014 (see Dauphas & Rouxel, 2006). Care was taken to match the concentration of standard and samples within 5%. Most of the samples were analyzed more than once to ensure reproducibility. The ^{54}Cr interference on ^{54}Fe was corrected using the intensity ^{53}Cr, which was generally about four orders less than the intensity of ^{54}Fe. The Fe isotope data is represented in 'δ'-notation relative to IRMM-014:

$$\delta^{56}Fe = \left[\frac{\left[\frac{^{56}Fe}{^{54}Fe} \right]_{sample}}{\left[\frac{^{56}Fe}{^{54}Fe} \right]_{standard}} - 1 \right] \times 1000 \text{ and } \delta^{57}Fe = \left[\frac{\left[\frac{^{57}Fe}{^{54}Fe} \right]_{sample}}{\left[\frac{^{56}Fe}{^{54}Fe} \right]_{standard}} - 1 \right] \times 1000$$

The analytical precision is ±0.12 ‰ (2σ, external) based on 76 measurements of IRMM-014 over three months while analyzing CIB nodules. The data from the literature, where cited, has been recalculated to IRMM-014 reference values for consistency.

2.4 Major and trace element analysis

An aliquot of the sample solution was analyzed for major and trace element analysis. Major elements Fe, Mn, Mg, Na, and K, were measured using AAS (Varian SpectrAA220) with pure elemental solutions and international standards (Nod-A1, Nod-P1, GSPN-2, GSPN-3, and IF-G). The relative standard deviation (% RSD) is <2 for all the elements. Trace elements, including the REEs, were analyzed using Thermo X Series 2 quadruple ICP-MS. The analytical accuracy for most elements is better than 5 (% RSD) and up to 7 % for a few low abundant elements, e.g., Be.

3. RESULTS

Major, trace element, and Fe isotope compositions of 16 CIB Mn-nodule and 3 Fe-Mn crust samples are presented in Table 1.

3.1 Major and Trace element compositions

The Mn and Fe concentrations in the analyzed CIB nodule scrapings range from 18.5 to 31.6 wt. % and 1.2 to 13.0 wt. %, respectively. The Mn/Fe values vary between 1.4 and 9.7. The alkali and alkaline earth elements (Mg, Na, and K) are all in low concentrations (< 3 wt. %), whereas Sr and Ba are moderately abundant. Ni and Cu are the most abundant among the transition elements, followed by Zn and Co (Table 1). Martin-Barajas et al. (1991) showed that the CIB Mn-Fe nodules plot in three distinct fields viz., hydrogenetic, on the Co-Ni-Cu ternary plot diagenetic and mixed. Samples from this study broadly conform to the above distribution, where

most nodules with the smooth surface plot in the 'hydrogenetic field' while those with rough (granular) surface plot either as 'diagenetic' or 'mixed' category (Fig. 2a). A similar distribution is also seen in the Mn-Fe-10(Ni+Cu+Co) ternary diagram for the samples in this study (Fig. 2b; after Bonatti et al., 1972). The three groups' samples show distinct Mn/Fe ratios: hyrogenetic from 1.4 to 3.3; mixed from 2.6 to 7.5 and diagenetic from 9.5 to 9.7 (Table 1). Further, in the Mn/Fe vs. Ni+Cu (%) plot, all samples from this study show a hyperbolic distribution suggestive of hydrogenetic origin (Mn/Fe ~ ≤ 1 and low Cu + Ni) and the influence of oxic diagenesis (higher Mn/Fe, Cu+Ni values) (Fig. 3; fields after Halbach et al., 1981). Interestingly there is no indication suggestive of the influence of sub-oxic diagenesis in our samples, unlike those from the Peru basin, where nodules with Mn/Fe ratios of >5 are depleted in Ni+Cu contents (<2 wt%, Glasby, 2006).

The nodule scrapings analyzed here show less fractionated REE patterns (normalized to Post-Archean Australian Shale; PAAS) with positive Ce anomalies $\left((Ce/Ce)^* = (Ce_N/\sqrt{La_N \times Pr_N})\right)$ (Fig. 4). The Ce anomalies of nodules vary from 1.2 to 4.0. The host siliceous sediments were also characterized by such positive Ce anomalies (Nath et al., 1992a). The middle REEs are enriched, consistent with previous results on whole-nodule REE compositions (Nath et al., 1992b; 1994; Pattan and Banakar, 1993). The Hydrogenetic nodules have the highest ΣREE relative to mixed and diagenetic types. The ΣREE of CIB nodules is negatively correlated with Mn/Fe (Fig. 5). The predominant hydrogenetic nature of the samples is evident in the plots of Gd vs. Ce_{SN}/Ce_{SN}^*, Y_{SN}/Ho_{SN} vs. Ce_{SN}/Ce_{SN}^*, Zr vs. Ce plots, and 100 (Zr+Y+Ce)-15(Cu+Ni)-(Mn+Fe)/4 ternary space (Fig. 6 a,b,c, d).

3.2 Fe isotope compositions

Overall, the δ^{56}Fe values of CIB manganese nodule samples define a range between –0.63 and –0.06 ‰ irrespective of their genetic affinity. In a plot of δ^{56}Fe vs. Mn/Fe (Fig. 7), the mixed nodules (nodules with diagenetic crust over hydrogenetic core) define a positive correlation, while the hydrogenetic nodules show a scatter. Notably, however, the three genetic types have distinct Mn/Fe ranges. Further, the δ^{56}Fe values of the mixed nodules show a positive correlation with Mn and other trace metals compatible with Mn-oxide phases (e.g., Li, Cu, Zn, Mo, Cd, Sb) (Fig. 8). They are negatively correlated with Fe concentrations and Fe-compatible trace metals such as Sc, Sn, Pb, Ge, Y, Zr, Nb, Hf, Th, Bi, and REEs (Fig. 9). The δ^{56}Fe values show a negative correlation with ΣREE and Ce/Ce* (Fig. 10 a,b).

3.3 Ferromanganese crusts

The Mn/Fe values of the three analyzed Fe-Mn crust samples vary between 0.7 and 3.1. The REE contents of Fe-Mn crust samples are higher than those in nodules with distinct enrichment in HREE (Fig. 4). Two crust samples (# SKC and AND) show positive Ce anomalies while the sample 'CIB' shows a negative one. The δ^{56}Fe values in three analyzed ferromanganese crust samples range from –0.55 to –0.12 ‰.

4. DISCUSSION

Important sources of Fe into the ocean (with corresponding δ^{56}Fe values) include: aerosol/eolian dust (δ^{56}Fe, ~ +0.1 ‰, Beard et al., 2003a; Waeles et al., 2007; Majestic et al., 2009), hydrothermal fluids (δ^{56}Fe, –0.1 to –1.5 ‰, Sharma et al., 2001, Beard et al., 2003b; Severmann et al., 2004; Rouxel et al., 2008b; Johnson et al., 2008; Tagliabue et al., 2010, 2014; Carazzo et al., 2013; Fitzsimmons et al., 2014; Saito et al., 2013; Resing et al. 2015) and dissolution related to oxic/sub-oxic

diagenesis of sediments (δ^{56}Fe, 0 to –3.45 ‰, Bergquist and Boyle, 2006; Severmann et al., 2006; 2008; John et al., 2012; Chever et al., 2015; Radic et al., 2011; Homoky et al., 2009; 2013). Therefore, the Fe isotope compositions of nodules/crusts are expected to result from varying proportions of input and the fractionation of Fe isotopes associated with each of these sources. In general, however, the mechanism of Fe isotope fractionation accounting for the observed ^{56}Fe depletion in Fe-Mn crusts and nodules remains enigmatic (see Levosseur et al., 2004; Chu et al., 2006). Arguably, the short residence time (τ) for Fe in seawater (~270 y; Bergquist et al., 2007) relative to the mixing time of the oceans (~1000 y; Broecker & Peng, 1982) imposes a limitation in invoking a significant role for Fe isotope fractionation between seawater and crust/nodule. Short residence time implies that the δ^{56}Fe values of nodules/crusts might relate to the dissolved Fe in the overlying water column (Chu et al., 2006). By contrast, Tl and Mo that have longer residence times than Fe in seawater record significant isotope fractionations during their transfer from seawater onto nodules (Rehkämper et al., 2002; Siebert et al., 2003). Chu et al. (2006) attempted to model the Fe isotope fractionation using the flow-through box model. They predicted that seawater and nodules attain equilibrium quickly such that the Fe isotope compositions of nodule/curst resemble dissolved Fe in the overlying water column. Adopting such a model and assuming i) $\delta^{56}Fe_{IN}$ = 0 ‰ (representing the Fe input to seawater) and ii) $\Delta_{CRUST/NODULE\text{-}DISSOLVED}$ (fractionation factor) = –0.77 ‰ (see below; after Horner et al., 2015), we obtain negative δ^{56}Fe values for the nodules with complementary positive values in seawater at the lower range of distribution coefficient (D) values (Fig. 11). However, an equilibrium with adjacent seawater is expected with increasing Fe flux.

The lack of correlation among $\delta^{56}Fe$ and various other elemental abundance in global Fe-Mn crusts/nodules are ascribed to factors such as variability in the provenance (Levosseur et al., 2004). A variety of sources were favored; eolian (Zhu et al., 2000; Marcus et al., 2015), a combination of eolian and hydrothermal (Beard et al., 2003a), and hydrothermal (Chu et al., 2006) with no significant fractionation of Fe isotopes during the transfer. Intriguingly, the dissolved Fe in deep oceans has $\delta^{56}Fe$ values typically range from +0.2 to +0.8 ‰ (Lacan et al., 2008; John & Adkins, 2010; Radic et al., 2011; Conway & John, 2014; Chever et al., 2015). Such a ^{56}Fe-enriched reservoir is an unlikely Fe source for the nodules/crusts considering their low $\delta^{56}Fe$ values. Also, with a dominantly eolian source ($\delta^{56}Fe$ ~ +0.1 ‰) (Conway & John, 2014), the Fe isotope compositions of nodules/crusts would require a fractionation mechanism for selective depletion of ^{56}Fe. In this context, preferential adsorption of ^{56}Fe onto organic ligands (siderophore complexes) as a viable mechanism for the Fe isotope fractionation appears pertinent. A fractionation factor ($\Delta^{56}Fe_{inorg\text{-}DFOB}$) of −0.6±0.15 ‰ between the Fe dissolved and adsorbed onto siderophore complexes under experimental conditions was estimated (Dideriksen et al., 2008). More recently, Horner et al. (2015) arrived at a fractionation factor of −0.77±0.06‰ ($\Delta^{56}Fe_{Fe\text{-}Mn\ crust\text{–}SW}$) based on the $\delta^{56}Fe$ values of selected Fe-Mn crusts and the spatially proximal dissolved Fe from the Pacific, which is close to the estimate of Dideriksen et al. (2008).

4.1 Source of Fe and isotope fractionation in hydrogenetic nodules

The CIB nodules (this study) show an average $\delta^{56}Fe$ value of –0.36±0.3 ‰ (2σ) broadly similar to global Fe-Mn oxides (average $\delta^{56}Fe$ = –0.41±0.49 ‰, 2 σ, Levasseur et al., 2004; Dauphas et al., 2017). The lack of correlation between $\delta^{56}Fe$ values and elemental abundance in the hydrogenetic group of nodules is akin to the

general observation of global nodule/crust data sets (cf. Levasseur et al., 2004). The low values of $\delta^{56}Fe$ of the CIB hydrogenetic nodules are consistent with the fractionation model involving selective adsorption of the heavier Fe isotopes onto organic ligands. There are no direct measurements for the Fe isotope composition of deep water dissolved Fe from the Indian Ocean. Assuming a fractionation factor of −0.77 ‰ (see above; after Horner et al., 2015), the range of $\delta^{56}Fe$ values of CIB hydrogenetic nodules from –0.14 to –0.49 ‰ constrain the Fe isotope composition of the dissolved Fe in the ambient ocean water at +0.28 to +0.63 ‰ much similar to those measured for the Atlantic Ocean deep waters (cf. Conway & John. 2014). Further, the latter range supports the view that the predominant Fe source into CIB may have been eolian with subsequent isotope fractionation mediated through adsorption onto organic ligands. Unlike in the Pacific Fe-Mn crust sample (CD29-2; Horner et al., 2015), the absence of $\delta^{56}Fe$ values >> 0 ‰ in the CIB hydrogenetic nodules precludes deeply sourced Fe, either hydrothermal source or its modification due to precipitation of sulfides enriched in the lighter Fe isotopes. The presence of organic ligands can be related to the primary productivity in the surface waters. Considering a mass balance between the dissolved and precipitated Fe represented as $\delta^{56}Fe_{IN} = (\delta^{56}Fe_{DISSOLVED} \times f_{DISSOLVED}) + (\delta^{56}Fe_{NODULE/CRUST} \times (1 - f_{DISSOLVED})$, where $f_{DISSOLVED}$ is the fraction of Fe dissolved in seawater and $\Delta^{56}Fe_{DISSOVLED\text{-}NODULE}$ = 0.77 ‰, it can be estimated that fraction of Fe transferred into nodule reservoir is 0.55±0.28 (1 σ) (Fig. 12 a). The average $\delta^{56}Fe$ of –0.41 ‰ for the global database indicates that a fraction of 0.47±0.45 (1 σ) of the total Fe is transferred onto nodules/crusts. However, this model assumes that the $\delta^{56}Fe$ of input Fe is ~ 0 ‰, but in a case where deeply sourced Fe such as the modified hydrothermal fluids assume prominence (see Horner et al., 2015), the actual fraction may vary. The Fe fractions

adsorbed onto organic ligands may be proportional to primary productivity in the different oceanic basins' surface water.

4.2 Source for Fe in the Mixed and Diagenetic nodule groups

The metal inventory in the CIB mixed group of nodules can be related to variable sourcing from diagenetic and hydogenetic fluxes. The mixed-mode nodules are characterized by an outer diagenetic crust and an interior with a hydrogenetic structure. Such a transition may reflect slow changes in the sedimentary environment during the nodule growth (Martin-Barajas et al., 1991). In general, during the oxic diagenesis of deep ocean sediments, Mn. Ni and Cu are released into the pore fluids, which eventually get incorporated into nodules forming at the sediment-water interface (e.g., Glasby, 2006). The diagenetic role manifests in the positive correlation between Mn/Fe and Cu+Ni (Fig. 3), where the CIB mixed group samples with higher Mn/Fe and Cu+Ni relate to an increasingly oxic diagenetic source. There is no Fe isotope data available for the pore fluids from the CIB nodule field. However, pore fluids from the Crozet deepwater region are similar to the CIB nodule field and show δ^{56}Fe close to 0 ‰ (Homoky et al., 2009). Expectedly, the δ^{56}Fe values of nodules having Fe from diagenetic sources would approach 0 ‰. In the case of CIB mixed group nodules, we interpret the linear correlations between δ^{56}Fe and various trace metals with affinity to Mn, Fe (Figs. 8 and 9) as mixing lines between the two endmembers representing hydrogenetic and diagenetic sources. The CIB nodule data are plotted along with the results of simple two-component mixing calculations (Fig. 12 b). Here, we assume endmember values of δ^{56}Fe = –0.77 ‰ for the hydrogenetic and δ^{56}Fe = 0 ‰ for diagenetic pore fluids (see discussion above). The computed Mn/Fe and δ^{56}Fe are shown for different proportions of the two endmembers at various Mn/Fe initial values [$(Mn/Fe)_i$]. The Fe's diagenetic source contribution in

mixed type nodules ranges from 19 to 91 %, and the $(Mn/Fe)_i$ of the diagenetic pore fluids vary between 2 and 4. On the other hand, the composition of the diagenetic nodules can be accounted for in terms of diagenetic contribution between 51 and 64 % at a high $(Mn/Fe)_i$ of ~6 for the pore fluid, which is consistent with the observation that Mn, Ni, Cu, Co are enriched in these nodules. From the preceding, it is evident that a large fraction of Fe in the CIB nodules, especially the mixed and diagenetic types, may have been sourced from diagenetic pore fluids. It would be interesting to assess this model's viability to nodules and crusts in other ocean basins, especially those with near 0‰ δ^{56}Fe compositions.

4.3 Fe-Mn crusts

The samples SKC and AND show positive Ce anomalies typical of hydrogenous Fe-Mn oxides (see Nath et al., 1994). The negative Ce anomaly in the sample 'CIB' is similar to those found in mixed hydrothermal-hydrogenous crusts from the Rodriguez Triple Junction (Nath et al., 1997), suggesting a hydrothermal source contribution (see also Fig. 6 d).

5. CONCLUSIONS

The polymetallic nodules constitute an extensive economic resource in the CIB. The nodules comprise distinct populations related to metal sourcing from hydrogenetic, diagenetic, and mixed sources. The range of δ^{56}Fe values in the CIB nodules is similar to that documented in Fe-Mn nodule/crust from different parts of the world ocean. The Fe isotope compositions of the CIB hydrogenetic nodules are consistent with a fractionation process involving selective adsorption of the heavy isotopes onto organic ligands (siderophoric complexes), resulting in their characteristic negative δ^{56}Fe isotope signatures. The mixed group of nodules from the

CIB exhibit compositional arrays attesting to variable proportions of metals from oxic diagenetic and hydrogenetic sources. This study from the Central Indian Basin nodule field brings forth relevance from diagenetic sources as an important component in the deep ocean's Fe biogeochemical cycling.

Acknowledgment

We thank the financial support from the Department of Science and Technology, CSIR, New Delhi and CSIR-NGRI, and CSIR-NIO in the establishment and operation of the MC-ICP-MS National Facility at CSIR-NGRI. We thank successive directors of CSIR-NGRI and CSIR-NIO for their encouragement and access to the nodule depositary. BS is grateful to Dr. T. Hirata, Kyoto University, Japan, for introducing the Fe isotope geochemistry at the Tokyo Institute of Technology. This work is part of the GENIAS project sanctioned by CSIR. Drs V.K. Banakar and R. Banerjee provided ferromanganese crust samples from the Afanasiy Nikitin seamount and the Central Indian Ridge. Datasets for this research are deposited with Earthcem repository and DOI will be mentioned once received.

References

Anbar, A.D., Roe J.E., Barling J., & Nealson K.H. (2000). Nonbiological fractionation of iron isotopes. *Science, 288*, 126–128.

Anbar, A.D., & Rouxel, O.J. (2007). Metal stable isotopes in paleoceanography. *Annual Review of Earth and Planetary Sciences, 35*, 717–746.

Banakar, V.K., & Borole, D.V. (1991). Depth profiles of $^{230}Th_{excess}$, transition metals and mineralogy of ferromanganese crusts of the Central Indian basin and implications for palaeoceanographic influence on crust genesis. *Chemical Geology, 94*, 33–44.

Bau, M., Schmidt, K., Koschinsky, A., Hein, J.R., & Usui, A. (2014). Discriminating between different genetic types of marine ferro-manganese crusts and nodules based on rare earth elements and yttrium. *Chemical Geology, 381,* 1–9.

Beard, B.L., Johnson C.M., von Damm, K.L. & Poulson, R. (2003a). Iron isotope constraints on Fe cycling and mass balanced in oxygenated Earth. *Geology, 31,* 629–632.

Beard, B.L., Johnson, C.M., Skulan, J.L., Nealson, K.H., Cox, L., & Sun, H. (2003b). Application of Fe isotopes to tracing the geochemical and biological cycling of Fe. *Chemical Geology, 195,* 87−117.

Bergquist, B., & Boyle, E. (2006). Iron isotopes in the Amazon River system: weathering and transport signatures. *Earth and Planetary Science Letters, 248,* 54−68.

Bergquist, B., Wu, J., & Boyle, E. (2007). Variability in oceanic dissolved iron is dominated by the colloidal fraction. *Geochimica et Cosmochimica Acta, 71,* 2960−2974.

Bonatti, E., Kraemer, T. & Rydell, H.S. (1972). Classification and genesis of submarine iron-manganese deposits. In D.R. Horn (Ed.) *Ferromanganese deposits on the ocean floor* (pp. 159−166). Washington DC: National Science Foundation.

Broecker, W.S., & Peng, T.-H. (1982). *Tracer in the Sea*. New York: Lamont-Doherty Geological Observation Publications, 690 pp.

Carazzo, G., Jellinek, A.M., & Turchyn, A.V. (2013). The remarkable longevity of submarine plumes: Implications for the hydrothermal input of iron to the deep-ocean. *Earth and Planetary Science Letters, 382,* 66–76.

Chever, F., Rouxel, O.J., Croot, P.L., Ponzevera, E., Wuttig, K., & Auro, M. (2015). Total dissolvable and dissolved iron isotopes in the water column of the Peru upwelling regime. *Geochimica et Cosmochimica Acta, 162,* 66−82.

Chu, N-C., Johnson C.M., Beard B.L., German C.R., Nesbitt R.W., & Frank, M. (2006). Evidence for hydrothermal venting in Fe isotope compositions of the deep Pacific Ocean through time. *Earth and Planetary Science Letters, 245,* 202−217.

Conway, T.M., & John, S.G. (2014). Quantification of dissolved iron sources in to the North Atlantic Ocean. *Nature, 511,* 212−215.

Dauphas, N., & Rouxel O.J. (2006). Mass spectrometry and natural variations of iron isotopes. *Mass Spectrometry Reviews, 25,* 545−550.

Dauphas, N., John, S.G., & Rouxel, O.J. (2017). Iron isotope systematics. In F-Z. Teng, J. Watkins, N. Dauphas (Eds.) *Non-Traditional Stable Isotopes, Reviews in Mineralogy and Geochemistry* (Vol. 82, pp. 415−510). Washington DC: Mineralagical Society of America and Geochemical Society.

DePaolo, D.J. (1981). Trace element and isotopic effects of combined wallrock assimilation and fractional crystallization. *Earth and Planetary Science Letters, 53,* 189–202.

476 Dideriksen, K., Baker, J.A., & Stipp, S.L.S. (2008). Equilibrium Fe isotope
477 fractionation between inorganic aqueous Fe(III) and the siderophore complex,
478 Fe(III)- desferrioxamine B. *Earth and Planetary Science Letters, 269,* 280–290.
479 Glasby, G.P. (2006). Manganese: predominant role of nodules and crusts. In H.D.
480 Schulz, M. Zabel (Eds.) *Marine geochemistry* (pp. 371–428). Berlin Heidelberg
481 New York: Springer.
482 Halbach, P., Scherhag, C., Hebisch, U., & Marchig, V. (1981). Geochemical and
483 mineralogical control of different genetic types of deep-sea nodules from Pacific
484 Ocean. *Mineralum Deposita, 16,* 59–84.
485 Homoky, W.B., Severmann, S., Mills, R.A., Statham P.J., & Fones G.R. (2009). Pore-
486 fluid Fe isotopes reflect the extent of benthic Fe redox recycling: Evidence from
487 continental shelf and deep-sea sediments. *Geology, 37,* 751–754.
488 Homoky, W.B., John, S.G., Conway, T.M., Mills, & R.A. (2013). Distinct iron
489 isotopic signatures and supply from marine sediment dissolution. *Nature*
490 *Communications, 4,* doi:10.1038/ncomms3143.
491 Horner, T.J., Williams, H.M., Hein, J.R., Saito, M.A., Burton, K.W., Halliday, A.N.
492 & Nielsen, S.G. (2015). Persistence of deeply sourced iron in the Pacific Ocean.
493 *Proceedigs of National Academy of Sciences, 112,* 1292–1297.
494 John, S.G., & Adkins, J.F. (2010). Analysis of dissolved iron isotopes in seawater.
495 *Marine Chemistry, 119,* 65–76.
496 Johnson, C.M., Beard, B.L., & Roden, E.E. (2008). The iron isotope fingerprints of
497 redox and biogeochemical cycling in modern and ancient Earth. *Annual Review of*
498 *Earth and Planetary Science Letters, 36,* 457–493.

499 Josso, P., Pelleter, E., Pourret, O., Fouquet Y., Etoubleaua J., Cheron S., & Bollinger
500 C., 2017. A new discrimination scheme for oceanic ferromanganese deposits
501 using high field strength and rare earth elements. *Ore Geology Reviews, 87,* 3–15.
502 Lacan, F., Radic, A., Jeandel, C., Poitrasson, F., Sarthou, G., & Pradoux, C. (2008).
503 Measurement of the isotopic composition of dissolved iron in the open ocean.
504 *Geophysical Research Letters, 35,* pp.L24610, doi:1-.1029/2008GL035841.
505 Levasseur, S., Frank, M., Hein, J.R., & Halliday, A., 2004. The global variation in the
506 iron isotope composition of marine hydrogenetic ferromanganese deposits:
507 implications for seawater chemistry. *Earth and Planetary Science Letters, 224,*
508 91–105.
509 Marcus, M.A., Edwards, K.J., Gueguen, B., Fakra, S.C., Horn, G., Jelinski, N.A.,
510 Rouxel, O., Sorensen, J., & Toner, B.M. 2015. Iron mineral structure, reactivity,
511 isotopic composition in a South Pacific Gyre ferromanganese nodule over 4 Ma.
512 *Geochimica et Cosmochimica Acta, 171,* 61−79.
513 Majestic, B.J., Anbar. A.D., & Herckes, P. (2009). Stable Isotopes as a Tool to
514 Apportion of Atmospheric Iron. *Environmental Science & Technology, 43,* 4327–
515 4333.
516 Marèchal, C.N., Telouk, P., & Albarède, F. (1999). Precise analysis of copper and
517 zinc isotopic composition by plasma-source mass spectrometry. *Chemical*
518 *Geology, 156,* 251–273.
519 Martin J.H., Gordon R.M., & Fitzwater S.E. (1990). Iron in Antarctic waters. *Nature,*
520 *345,* 156–158.
521 Martin-Barajas, A., Lallier-Verges, E., & Leclaire, L. (1991). Characteristics of
522 manganese Basin: Relationship with the sedimentary environment. *Marine*
523 *Geology, 101,* 249-265.

524 Mukhopadhyay, R., & Nath, B.N. (1988). Influence of seamount topography on the
525 local facies variation in ferromanganese deposits from the Indian Ocean. *Deep-*
526 *Sea Research, 35,* 1431–1436.
527 Mukhopadhyay, R., George P., & Ranade, G. (1997). Spreading rate dependent
528 seafloor deformation in response to Inda-Eurasia collision: Results of hydrosweep
529 survey in the Central Indian Ocean Basin. *Marine Geology, 140,* 219–229.
530 Mukhopadhyay, R., Iyer, S.D., & Ghosh. A.K. (2002). The Indian Ocean nodule field:
531 Petrotectonic evolution and ferromanganese deposits. *Earth Science Reviews, 60,*
532 67–130.
533 Mukhopadhyay, R., Ghosh, A.K., & Iyer, S.D. (2008). *The Indian Ocean nodule*
534 *field: Geology and Resource Potential*. Amsterdam: Elsevier Publ. 292pp.
535 Nath, B.N., Rao V.P.C., & Becker, K.P. (1989). Geochemical evidence of terrigenous
536 influence in deep-sea sediments up to 8°S in the Central Indian Basin. *Marine*
537 *Geology, 87,* 301–313.
538 Nath, B.N., Roelandts, I., Sudhakar, M., & Pluger, W.L. (1992a). Rare earth element
539 patterns of the Central Indian Basin sediments related to their lithology.
540 *Geophysical Research Letters, 19,* 1197–1200.
541 Nath, B.N., Balaram, V., Sudhakar, M., & Pluger, W.L. (1992b). Rare earth element
542 geochemistry of ferromanganese deposits from the Indian Ocean. *Marine*
543 *Chemistry, 38,* 185–208.
544 Nath, B.N., Roelandts, I., Sudhakar, M., Plüger, W.L., & Balaram V. (1994). Cerium
545 anomaly variations in ferromanganese nodules and crusts from the Indian Ocean.
546 *Marine Geology, 120,* 385–400.
547 Nath, B.N., Plüger, W.L., & Roelandts, I. (1997). Geochemical constraints on the
548 hydrothermal origin of ferromanganese encrustations from the Rodriguez Triple

549 Junction, Indian Ocean. In K. Nicholson, J.R. Hein, B. Bühn, S. Dasgupta (Eds.)
550 *Manganese Mineralization: Geochemistry and Mineralogy of Terrestrial and*
551 *Marine Deposits Geological Society (London) Special Publications* (Vol. 119,
552 pp.199–211). London: Geological Society (London).
553 Pattan, J.N., & Banakar, V.K. (1993). Rare earth element distribution and behavior in
554 buried manganese nodules from the Central Indian Basin. *Marine Geology, 112,*
555 303–312.
556 Pimm, A.C. (1974). Sedimentology and history of the northeastern Indian Ocean from
557 late Cretaceous to Recent. *lnitial Reports DSDP, 22,* 717–804.
558 doi:10.2973/dsdp.proc.22.139.1974.
559 Radic, A., Lacan, F., & Murray, J.W. (2011). Iron isotopes in the seawater of the
560 equatorial Pacific Ocean; New constraints for the oceanic iron cycle. *Earth and*
561 *Planetary Science Letters, 306,* 1–10.
562 Rehkamper, M., Frank, M., Hein, J.R., Porcelli, D., Halliday, A.N., Ingri, J., &
563 Liebetrau V. (2002). Thallium isotope variations in seawater and hydrogenetic,
564 diagenetic, and hydrothermal ferromanganese deposits. *Earth and Planetary*
565 *Science Letters, 197,* 65–81.
566 Resing, J.A., Sedwick, P.N., German, C.R., Jenkins, W.J., Moffett, J.W., Sohst, B.M.,
567 & Tagliabue, A. (2015). Basin-scale transport of hydrothermal dissolved metals
568 across the South Pacific Ocean. *Nature, 523,* 200–203.
569 Rouxel, O.J., Sholkovitz, E., Charette, M., & Edwards, K.J. (2008a). Iron isotope
570 fractionation in subterranean estuaries. *Geochimica et Cosmochimica Acta, 72,*
571 3413–3430.

572 Rouxel, O.J., Shanks, W.C., Bach, W., & Edwards, K.J. (2008b). Integrated Fe- and
573 S-isotope study of seafloor hydrothermal vents at East Pacific rise 9–10°N.
574 *Chemical Geology, 252,* 214–227.
575 Royer, J.Y., Sclater, J.G., Sandwell, D.T., & Cande S.C. (1989). A preliminary
576 tectonic fabric chart of the Indian Ocean. *Proceedings Indian Academy of*
577 *Sciences, 98,* 7–24.
578 Saito, M.A., Noble, A.E., Tagliabue, A., Goepfert, T.J., Lamborg, C.H., & Jenkins,
579 W.J. (2013). Slow-spreading submarine ridges in the South Atlantic as a
580 significant oceanic iron source. *Nature Geoscience, 6,* 775–779.
581 Siebert, C., & Nägler, T.F., von Blanckenburg, F., Kramers, J.D. (2003).
582 Molybdenum isotope records as a potential new proxy for paleoceanography,
583 *Earth and Planetary Science Letters, 211,* 159–171.
584 Severmann, S., Johnson C.M., Beard B.L., German, C.R., & Edmonds, H.N. (2004).
585 The effect of plume processes on the Fe isotope composition of hydrothermally
586 derived Fe in the deep ocean as inferred from the Rainbow vent site, Mid-Atlantic
587 Ridge, 36 degrees 14 N. *Earth and Planetary Science Letters, 225,* 63–76.
588 Severmann, S., Johnson, C.M., Beard, B.L., & McManus, J. (2006). The effect of
589 early diagenesis on the Fe isotope compositions of porewaters and authigenic
590 minerals in continental margin sediments. *Geochimica et Cosmochimica Acta, 70,*
591 2006–2022.
592 Severmann, S., Lyons T.W., Anbar, A.D., McManus, J., & Gordon G. (2008).
593 Modern iron isotope perspective on the benthic iron shuttle and the redox
594 evolution of ancient oceans. *Geology, 36,* 487–490.
595 Sharma, M., Polizzotto, M., & Anbar, A.D. (2001). Iron isotopes in hot springs along
596 the Juan de Fuca Ridge. *Earth and Planetary Science Letters, 194,* 39–51.

Tagliabue, A., Bopp, L., Dutay, J.C., Bowie, A.R., Chever, F., Jean-Baptiste, P., Bucciarelli, E., Lannuzel, D., Remenyi, T., Sarthou, G., & Aumont, O. (2010). Hydrothermal contribution to the oceanic dissolved iron inventory. *Nature Geoscience, 3,* 252–256.

Tagliabue, A., Aumont, O., & Bopp, L. (2014). The impact of different external sources of iron on the global carbon cycle. *Geophysical Research Letters, 41,* 920–926.

Taylor, S.R., & McLennan, S.M. (1985). *The Continental Crust: Its Composition and Evolution.* Carlton: Blackwell Publications, 312pp.

Vineesh, T.C., Nath B.N., Banerjee R., Jaisankar S., & Lekshmi, V. (2009). Manganese nodule morphology as indicators for oceanic processes in the Central Indian Basin. *International Geology Reviews, 51,* 27–44.

Vereshchagin, O.S., Perova, E.N., Brusnitsyn, A.I., Ershova, V.B., Khudoley, A.K., Shilovskikh, V.V., & Molchanova, E.V. (2019). Ferro-manganese nodules from the Kara Sea: mineralogy, geochemistry and genesis, *Ore Geology Reviews, 106,* 192–204. DOI: https://doi.org/10.1016/j.oregeorev.2019.01.023.

von Stackelberg, U., & Marchig, V. (1987). Manganese nodules from the equatorial North Pacific Ocean. *Geologisches Jahrbuch, 87D,* 123–227.

Waeles, M., Baker, A.R., Jickells, T., & Hoogewerff., J. (2007). Global dust teleconnections: aerosol iron solubility and stable isotope composition. *Environmental Chemistry, 4,* 233–237.

Zhu, X.K., O'Nions, K., Guo, Y., & Reynolds, B.C. (2000). Secular variation of iron isotopes in North Atlantic deep water. *Science, 287,* 2000–2002.

620 **Figure captions**

621 **Figure 1 (a)** The bathymetric map of the part of the Indian Ocean showing the CIB
622 (CLR – Chagos Laccadive Ridge; NER – Ninetyeast Ridge). The yellow rectangle is
623 enlarged in **(b)** showing the locations of manganese nodules and ferromanganese
624 crusts of the present study overlain on sediment distribution in the CIB. The δ^{56}Fe
625 value (‰ IRMM-014) of each of the nodule/crust samples is given above the sample
626 location.

627 **Figure 2 (a)** Co-Ni-Cu ternary diagram for the CIB nodules and crusts showing the
628 correspondence of smooth and rough-textured nodules with hydrogenetic, mixed, and
629 diagenetic affinities (fields after Martin-Barajas et al., 1991). **(b)** Mn-Fe-
630 10(Cu+Ni+Co) ternary plot for manganese nodule and Fe-Mn crust samples (fields
631 after Bonatti et al., 1972). The mixed and diagenetic nodules plot closer to Mn–
632 10(Cu+Ni+Co) join, indicating a diagenetic source for these metals.

633 **Figure 3** Mn/Fe vs. (Cu+Ni) plot of manganese nodule and crust samples. The array
634 is similar to the regression of Peru Basin nodules (PB I nodules) than that of the
635 Clarion Clipperton Zone (CCZ) nodules. Hydrogenetic nodules have low Mn/Fe and
636 (Cu+Ni) values, while Mixed nodules have characters similar to those affected by
637 oxic diagenesis. Notably, the diagenetic nodules with high Mn/Fe values (> 9) exhibit
638 high (Cu+Ni) values of > 2.5, indicating that they were also affected by diagenesis.
639 However, it is noticeable that the reversal in (Cu+Ni) values at Mn/Fe of ~ 5 that was
640 observed, especially in Peru Basin nodules due to the influence of sub-oxic diagenesis
641 (PB II nodules; Glasby, 2006) is not found in the case of CIB nodules.

642 **Figure 4** PAAS normalized (normalization values after Taylor and McLennan, 1985)
643 REE patterns of manganese nodules and crust samples from the CIB. The
644 Hydrogenetic nodules are represented with dark grey dashed lines with various

symbols. The mixed group of nodules is shown with light grey dashed-dotted lines. The diagenetic group of nodules are shown with medium grey dotted lines. The crust samples are shown as solid black lines. Note positive Ce anomalies and slight middle REE enrichment in the nodules.

Figure 5 Mn/Fe vs. ΣREE contents showing a correlation controlled by a power law.

Figure 6 a) Gd vs. Ce_{SN}/Ce_{SN}*, **b)** Y_{SN}/Ho_{SN} vs. Ce_{SN}/Ce_{SN}* (subscript SN refers to PAAS normalized ratios) (fields after Bau et al., 2014), **(c)** Zr vs. Ce plot of CIB nodules and crusts (fields after Vereshchagin et al., 2019) and **(d)** 100 (Zr+Y+Ce)-15(Cu+Ni) -(Mn+Fe)/4 diagram (fields after Josso et al., 2017) of CIB nodule and crust samples.

Figure 7 Mn/Fe vs. δ^{56}Fe values of manganese nodule and ferromanganese crust samples of the CIB. The Mixed group of nodules shows an exponential correlation. Such a correlation is not noticed in Hydrogenetic nodules.

Figure 8 δ^{56}Fe vs. Mn, Li, Cu, Zn, Mo, Cd plots showing positive correlations for Mixed group of nodules and R^2 values are also given. It can be observed that with an increase in Mn, the δ^{56}Fe values become higher, indicating that the observed correlations are because of two-component mixing.

Figure 9 δ^{56}Fe vs. Fe, Be, Sc, Co, Zr, Nb plots showing negative correlations for the Mixed group of nodules.

Figure 10 δ^{56}Fe vs. **(a)** ΣREE and **(b)** Ce/Ce* showing negative correlations similar to the Fe and Fe-related trace metals.

Figure 11 Simple flow-through "box model" for estimating the Fe isotope fractionation associated with the transfer of Fe^{3+} from seawater onto crust/nodule surface (after DePaolo, 1981; Chu et al., 2006). The "box" refers to an arbitrary volume of ambient water adjacent to Fe-Mn crust/nodule. The model assumes: (i)

incoming Fe flux (J_{IN}) is equal to the outgoing flux (J_{OUT}) from seawater; (ii) the Fe concentration of intermediate reservoir remains constant and (iii) the $\delta^{56}Fe$ of the intermediate reservoir is equal to that of the incoming flux ($\delta^{56}Fe_{IN}$). The fractionation between seawater and Fe-Mn crust/nodule ($\Delta_{CRUST/NODULE\text{-}SEAWATER} = \delta^{56}Fe_{CRUST} - \delta^{56}Fe_{SW}$). The precipitation progress (R) is defined as the mass ratio of incoming flux and ambient seawater (M_{IN}/M_{SW}) and the Fe distribution coefficient (D) as $C_{CRUST/NODULE}/C_{SW}$ (where C is Fe concentration). $\delta^{56}Fe_{SW} = \delta^{56}Fe_{IN} - \Delta_{CRUST\text{-}SW} \times [1 - \exp(-D \times R)]$ and, for instantaneous $\delta^{56}Fe_{CRUST} = \Delta_{CRUST\text{-}SW} + \delta^{56}Fe_{SW}$ (see Chu et al., 2006). We have assigned $\delta^{56}Fe_{IN}$ = 0 ‰ and $\Delta_{CRUST\text{-}SEAWATER}$ = −0.77 ‰.

Figure 12 (a) Plot of $\delta^{56}Fe$ vs f_{nod} calculated using the mass balance equation: $\delta^{56}Fe_{IN} = (\delta^{56}Fe_{DISSOLVED} \times f_{DISSOLVED}) + (\delta^{56}Fe_{NODULE/CRUST} \times (1 - f_{DISSOLVED})$, where $f_{DISSOLVED}$ = the fraction iron in dissolved state. $f_{nod} = 1 - f_{DISSOLVED}$ and $\Delta^{56}Fe_{DISSOVLED\text{-}NODULE}$ = 0.77 ‰. The average $\delta^{56}Fe$ values for the CIB nodules (dark dot) and that of the global Fe-Mn crusts (grey dot) are also plotted. **(b)** Two component mixing model for estimating the diagenetic contribution. The black curves at different $(Mn/Fe)_i$ values show $\delta^{56}Fe$ variation as a result of mixing two endmembers viz. hydrogenetic (–0.77 ‰) and diagenetic (0 ‰) sources. Also plotted are the Mn/Fe and $\delta^{56}Fe$ values of CIB nodules.

Figure.

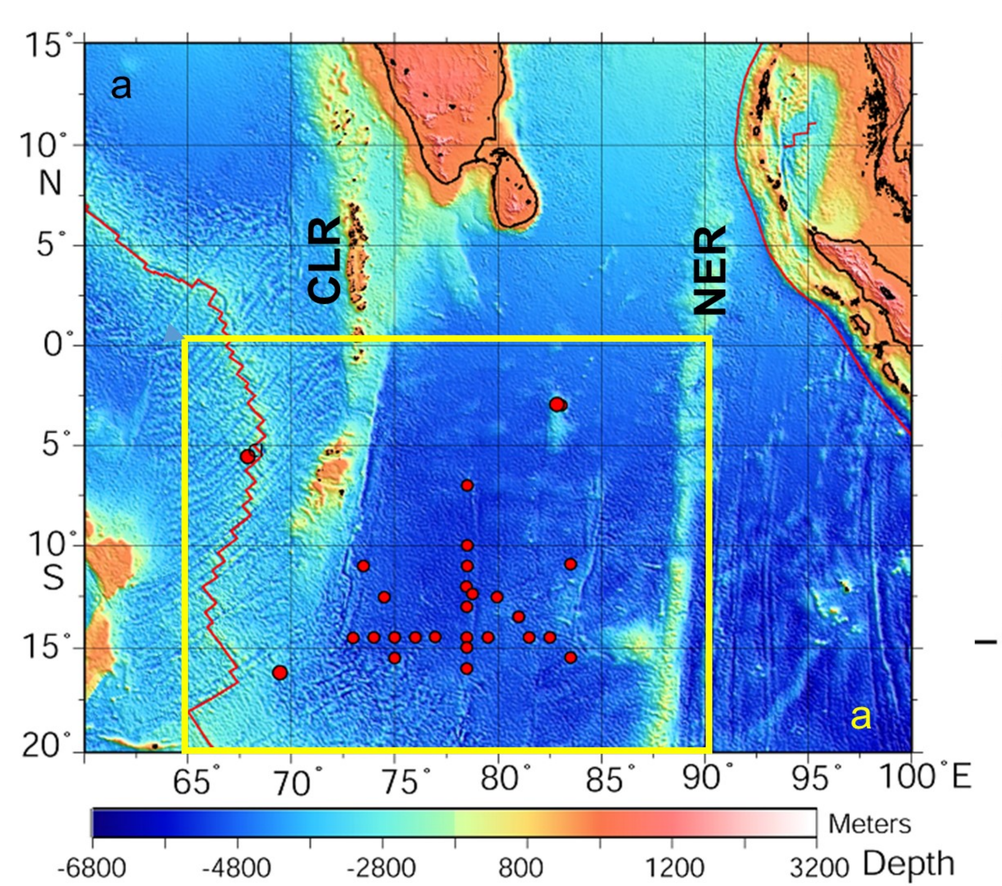
a
CLR
NER
15°
10° N
5°
0°
5°
10° S
15°
20°
65°
70°
75°
80°
85°
90°
95°
100°E
Meters
-6800
-4800
-2800
800
1200
3200
Depth

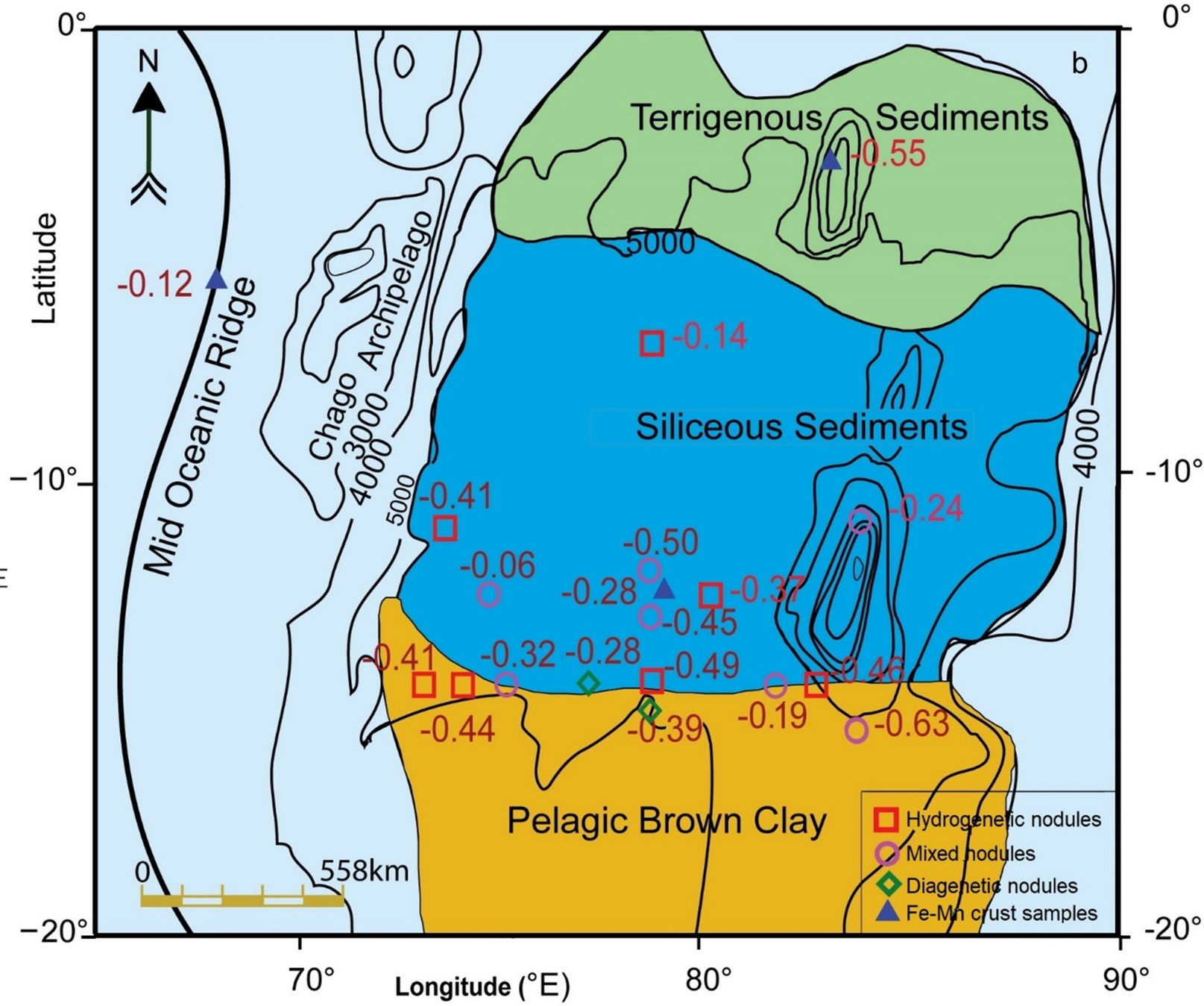
b
N
0°
−10°
−20°
Latitude
70°
80°
90°
Longitude (°E)
Terrigenous Sediments
Siliceous Sediments
Pelagic Brown Clay
Mid Oceanic Ridge
Chago Archipelago
5000
4000
3000
4000
5000
-0.12
-0.55
-0.14
-0.41
-0.24
-0.50
-0.06
-0.28
-0.37
-0.45
-0.41
-0.32
-0.28
-0.49
-0.46
-0.44
-0.39
-0.19
-0.63
0
558km
Hydrogenetic nodules
Mixed nodules
Diagenetic nodules
Fe-Mn crust samples

Figure.

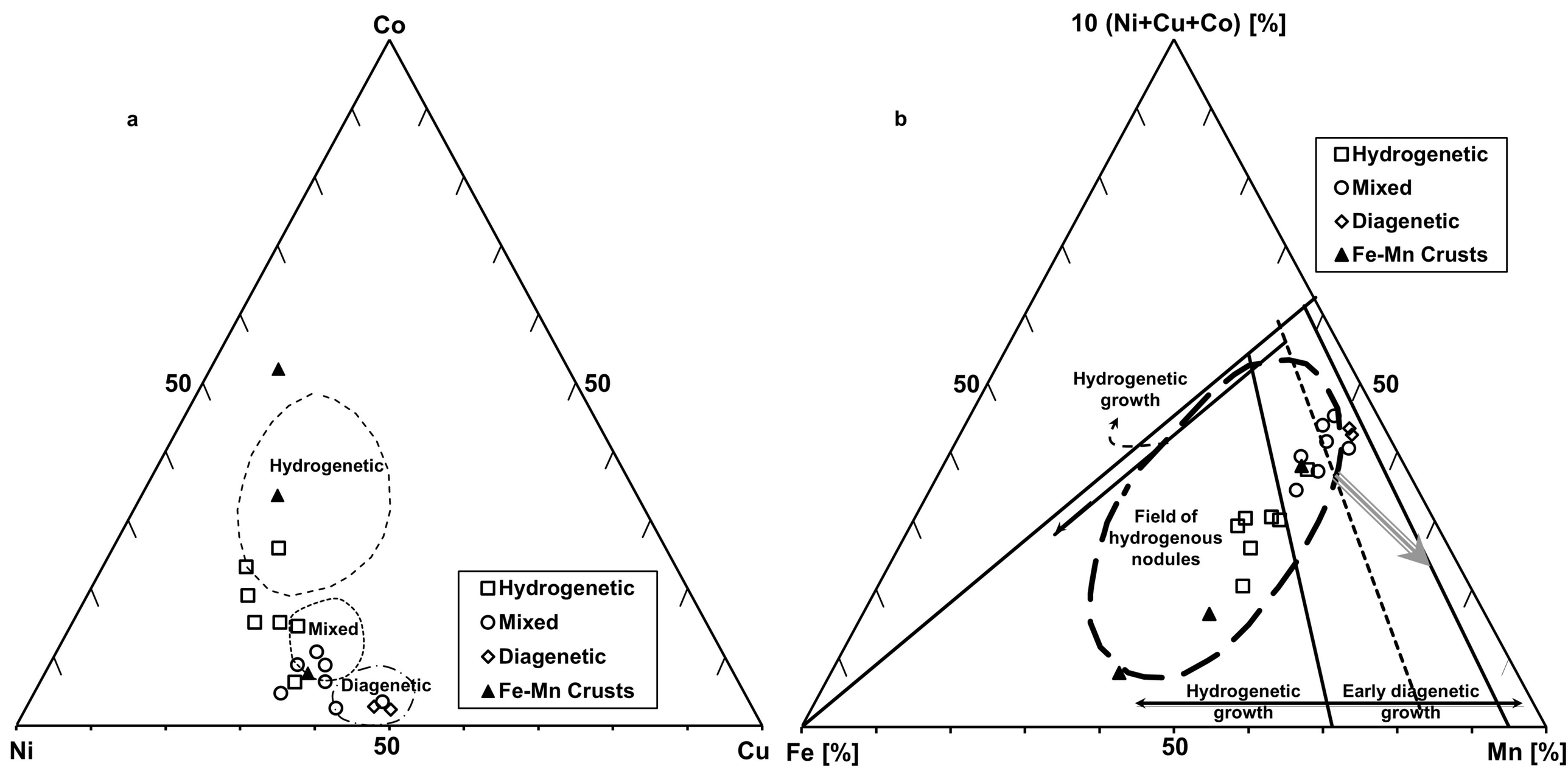
a
Co
50
50
Ni
50
Cu
Hydrogenetic
Mixed
Diagenetic
Hydrogenetic
Mixed
Diagenetic
Fe-Mn Crusts
b
10 (Ni+Cu+Co) [%]
50
50
Fe [%]
50
Mn [%]
Hydrogenetic
Mixed
Diagenetic
Fe-Mn Crusts
Hydrogenetic growth
Field of hydrogenous nodules
Hydrogenetic growth
Early diagenetic growth

Figure.

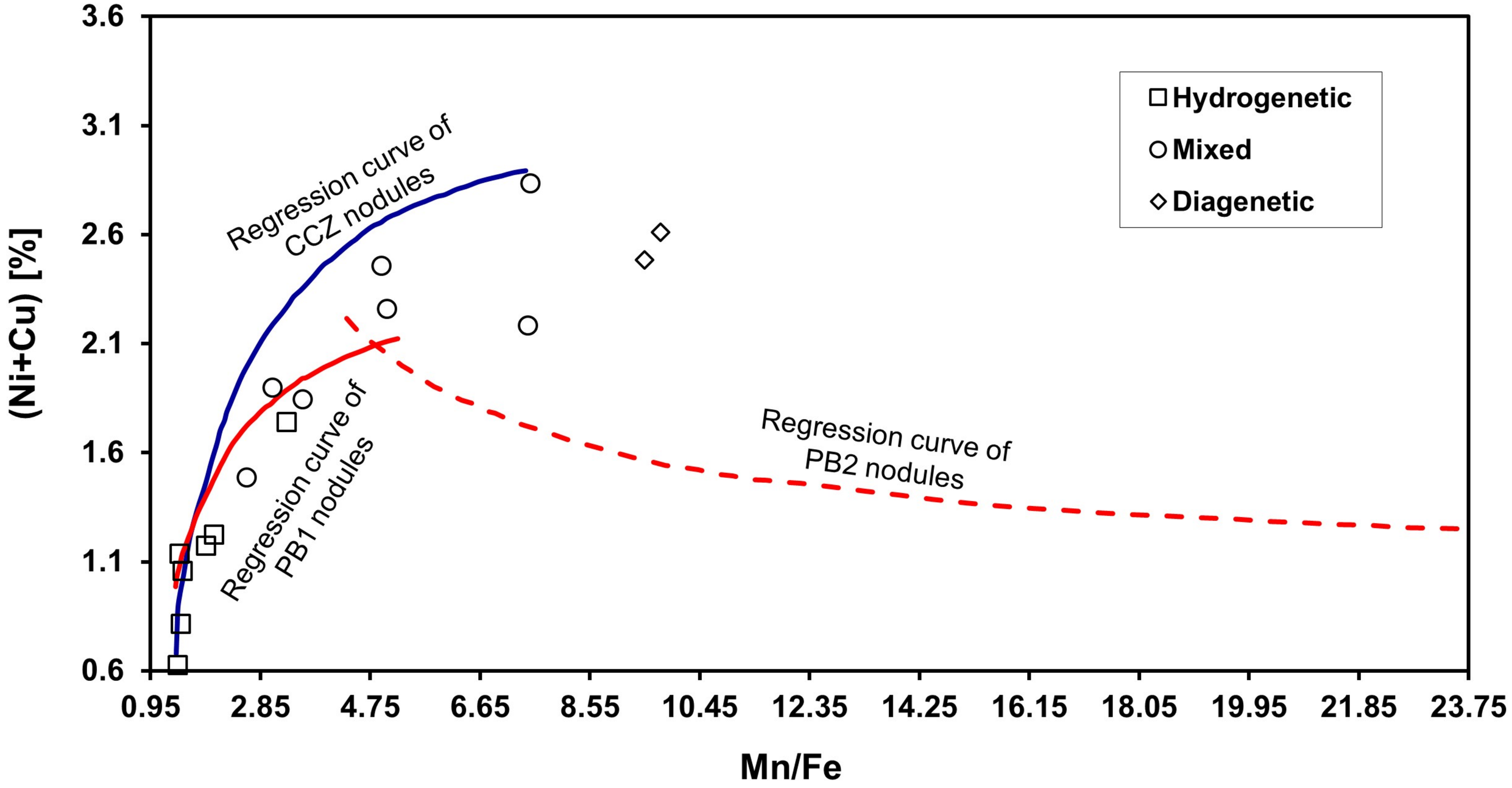
3.6
3.1
2.6
2.1
1.6
1.1
0.6
(Ni+Cu) [%]
0.95
2.85
4.75
6.65
8.55
10.45
12.35
14.25
16.15
18.05
19.95
21.85
23.75
Mn/Fe
Hydrogenetic
Mixed
Diagenetic
Regression curve of CCZ nodules
Regression curve of PB1 nodules
Regression curve of PB2 nodules

Figure.

F-1-13-TLS
F-3-155-TLS
S-3-191-TLS
S-3-203-TLS
S-4-227-TLS
S-4-229-TLS
S-7-328-TLS
S-211-TLS
S-3-144-TLS
S-3-180-TLS
S-3-201-TLS
S-4-225-TLS
SK-11-93-TLS
R-171-TLS
S-4-260-TLS
SK-8-56-TLS
AND
CIB
SKC

100
10
1
Nodule/PAAS
La
Ce
Pr
Nd
Sm
Eu
Gd
Tb
Dy
Ho
Er
Tm
Yb
Lu

Figure.

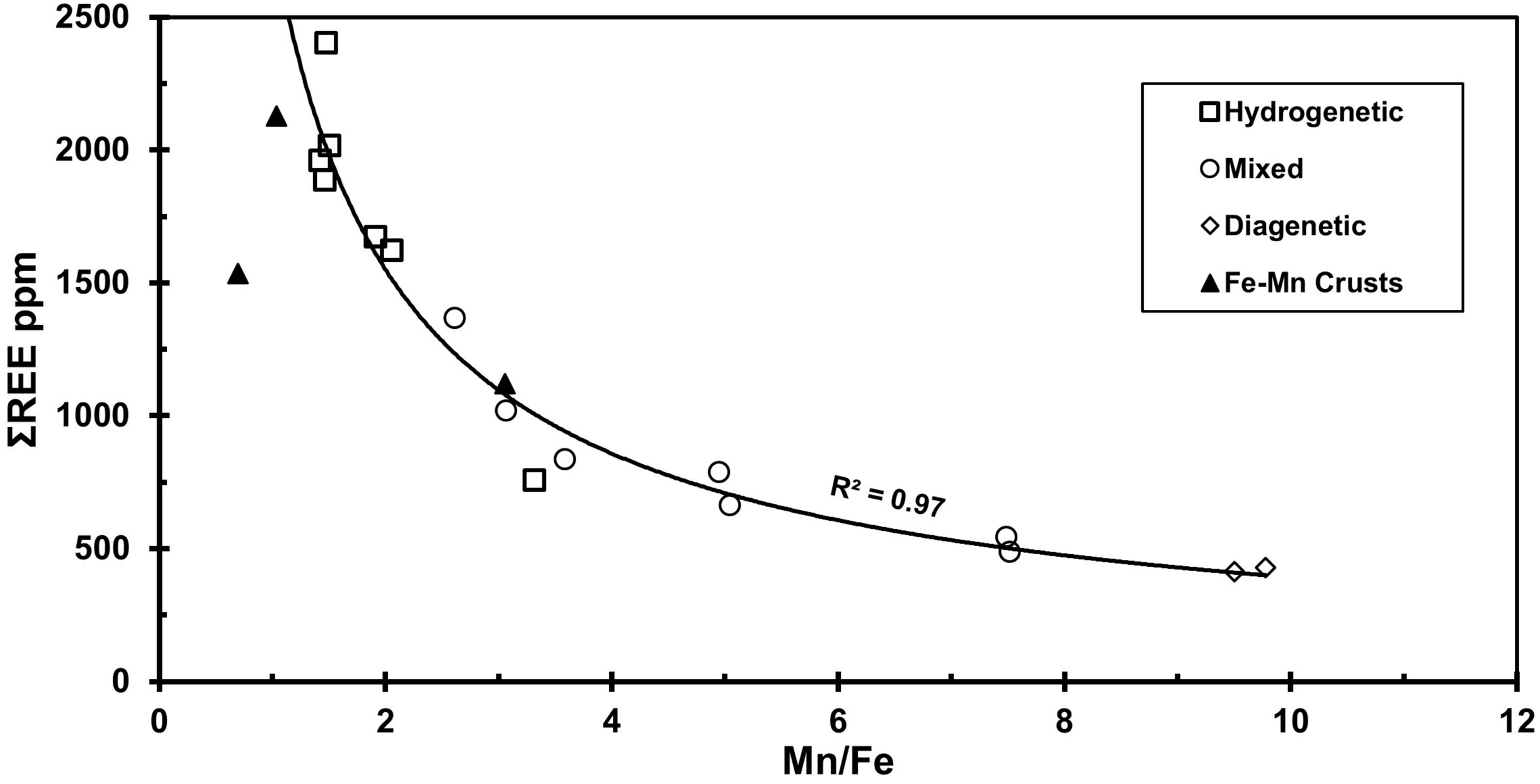
2500
2000
1500
1000
500
0
ΣREE ppm
0
2
4
6
8
10
12
Mn/Fe
Hydrogenetic
Mixed
Diagenetic
Fe-Mn Crusts
R² = 0.97

Figure.

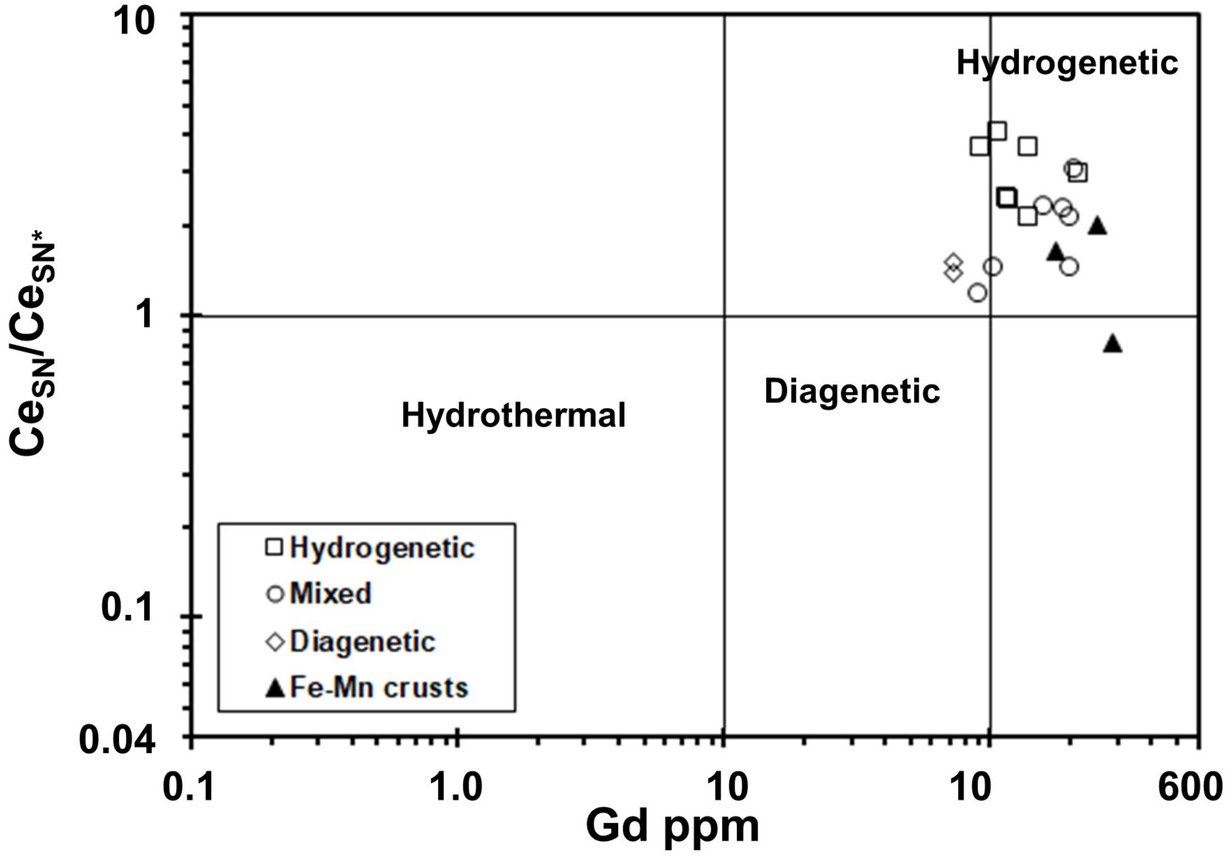
10
1
0.1
0.04
0.1
1.0
10
10
600
Gd ppm
Ce$_{SN}$/Ce$_{SN*}$
Hydrogenetic
Hydrothermal
Diagenetic
Hydrogenetic
Mixed
Diagenetic
Fe-Mn crusts

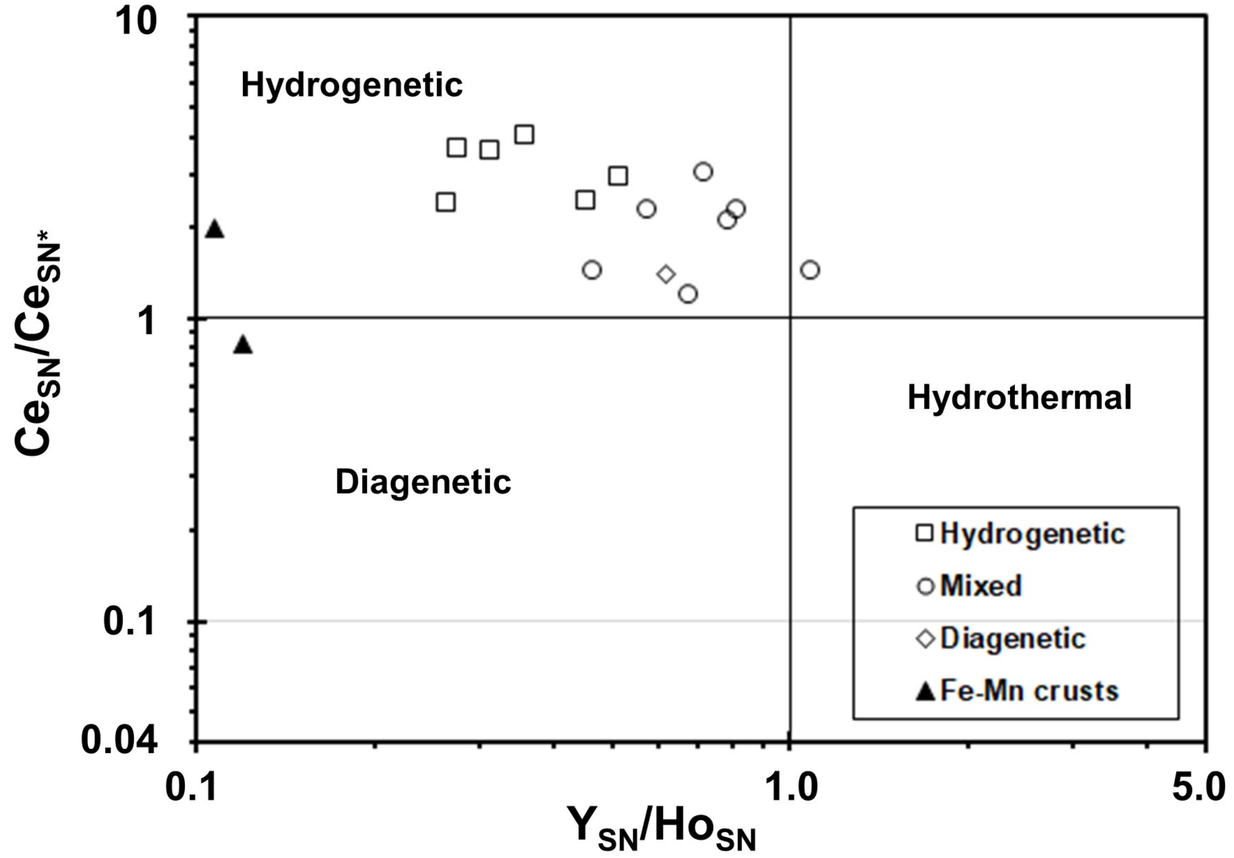
10
1
0.1
0.04
0.1
1.0
5.0
Y$_{SN}$/Ho$_{SN}$
Ce$_{SN}$/Ce$_{SN*}$
Hydrogenetic
Hydrothermal
Diagenetic
Hydrogenetic
Mixed
Diagenetic
Fe-Mn crusts

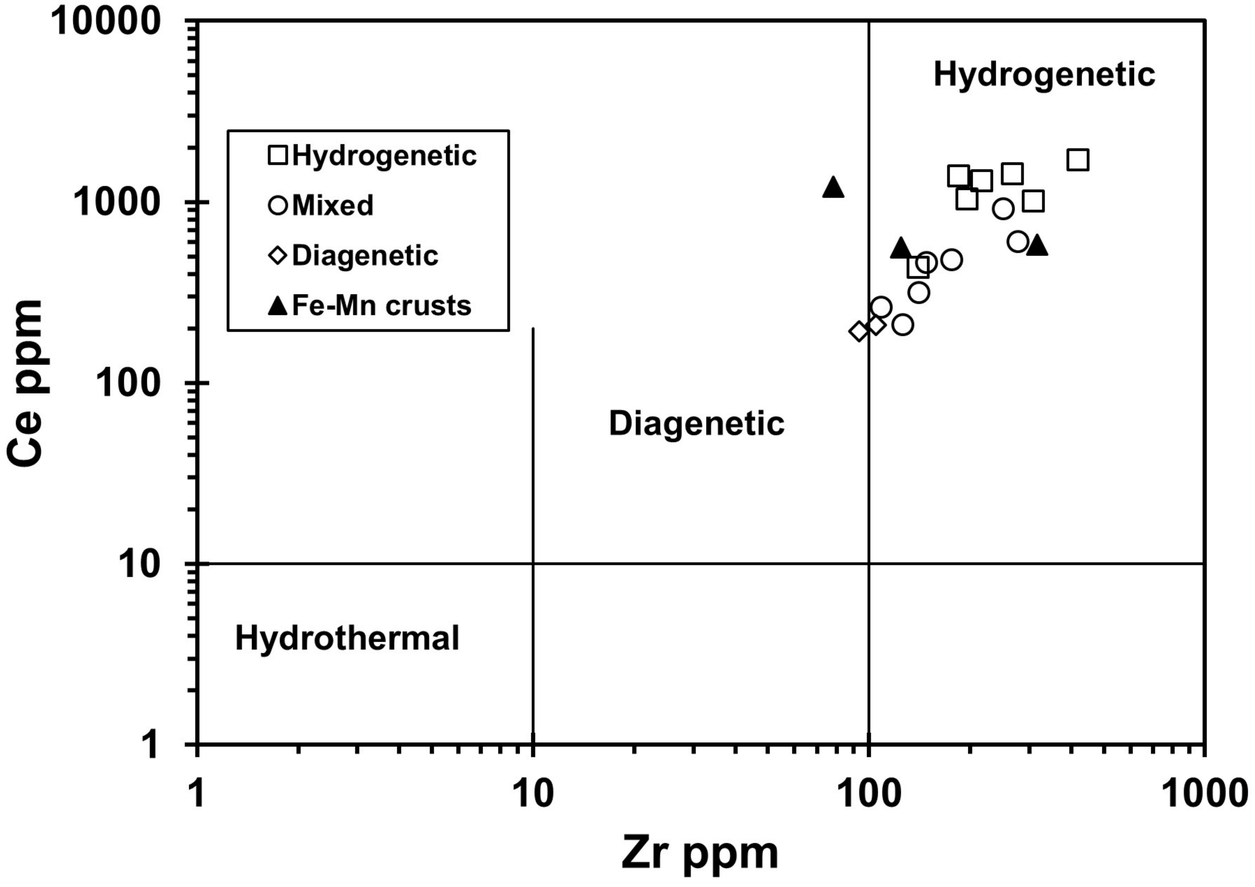
10000
1000
100
10
1
1
10
100
1000
Zr ppm
Ce ppm
Hydrogenetic
Mixed
Diagenetic
Fe-Mn crusts
Hydrogenetic
Diagenetic
Hydrothermal

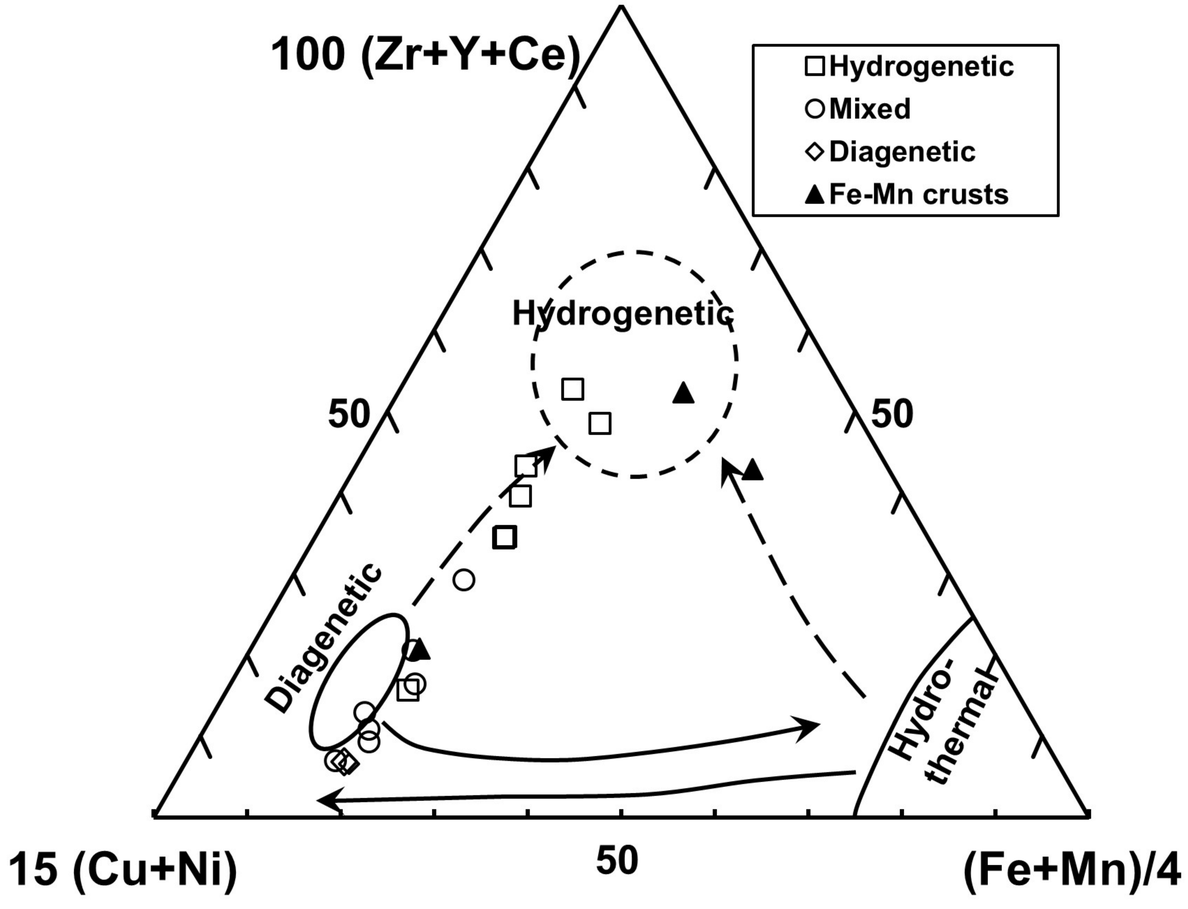
100 (Zr+Y+Ce)
15 (Cu+Ni)
50
(Fe+Mn)/4
50
50
Hydrogenetic
Mixed
Diagenetic
Fe-Mn crusts
Hydrogenetic
Diagenetic
Hydro-
thermal

Figure.

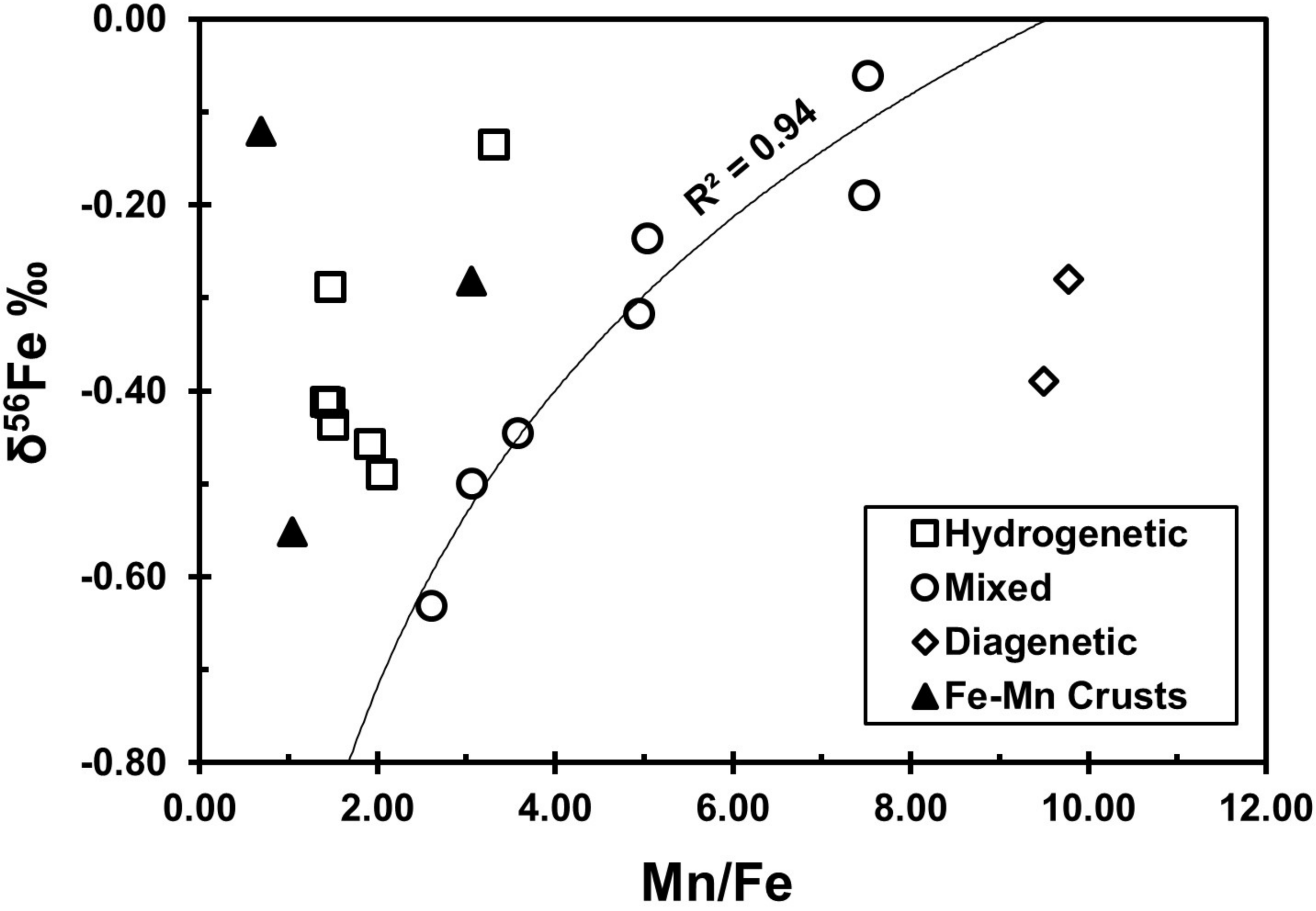
0.00
-0.20
-0.40
-0.60
-0.80
δ56Fe ‰
R² = 0.94
Hydrogenetic
Mixed
Diagenetic
Fe-Mn Crusts
0.00
2.00
4.00
6.00
8.00
10.00
12.00
Mn/Fe

Figure.

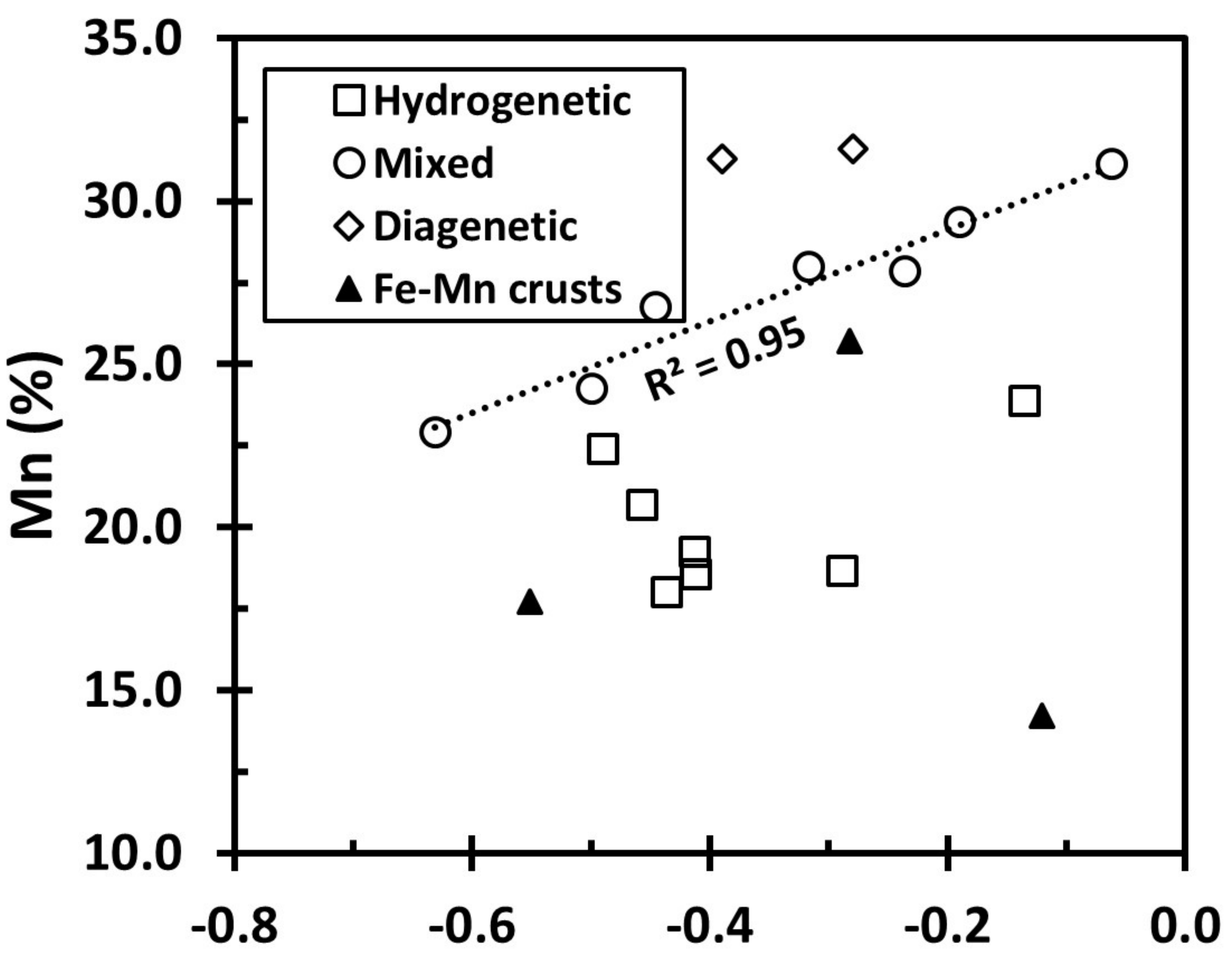

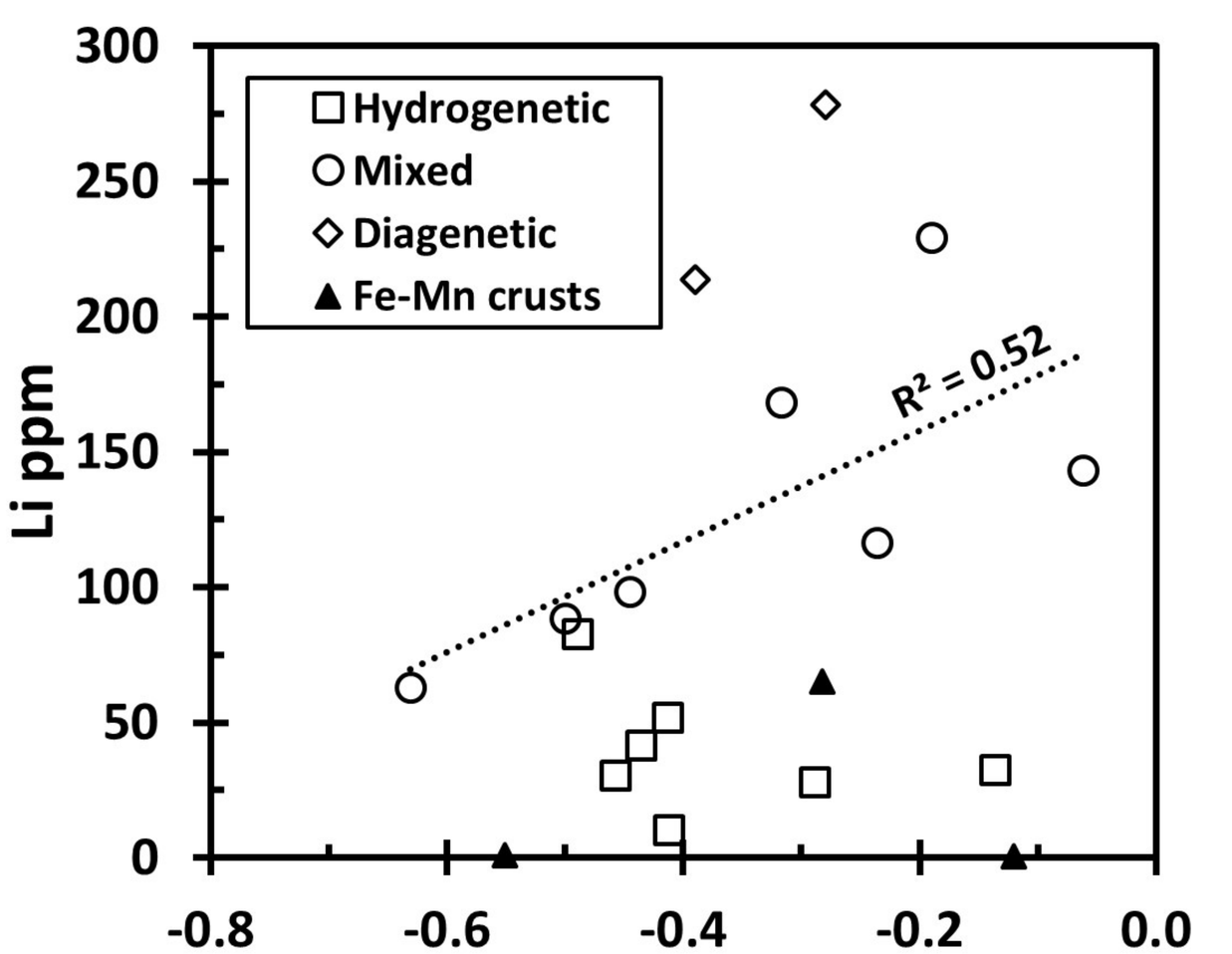

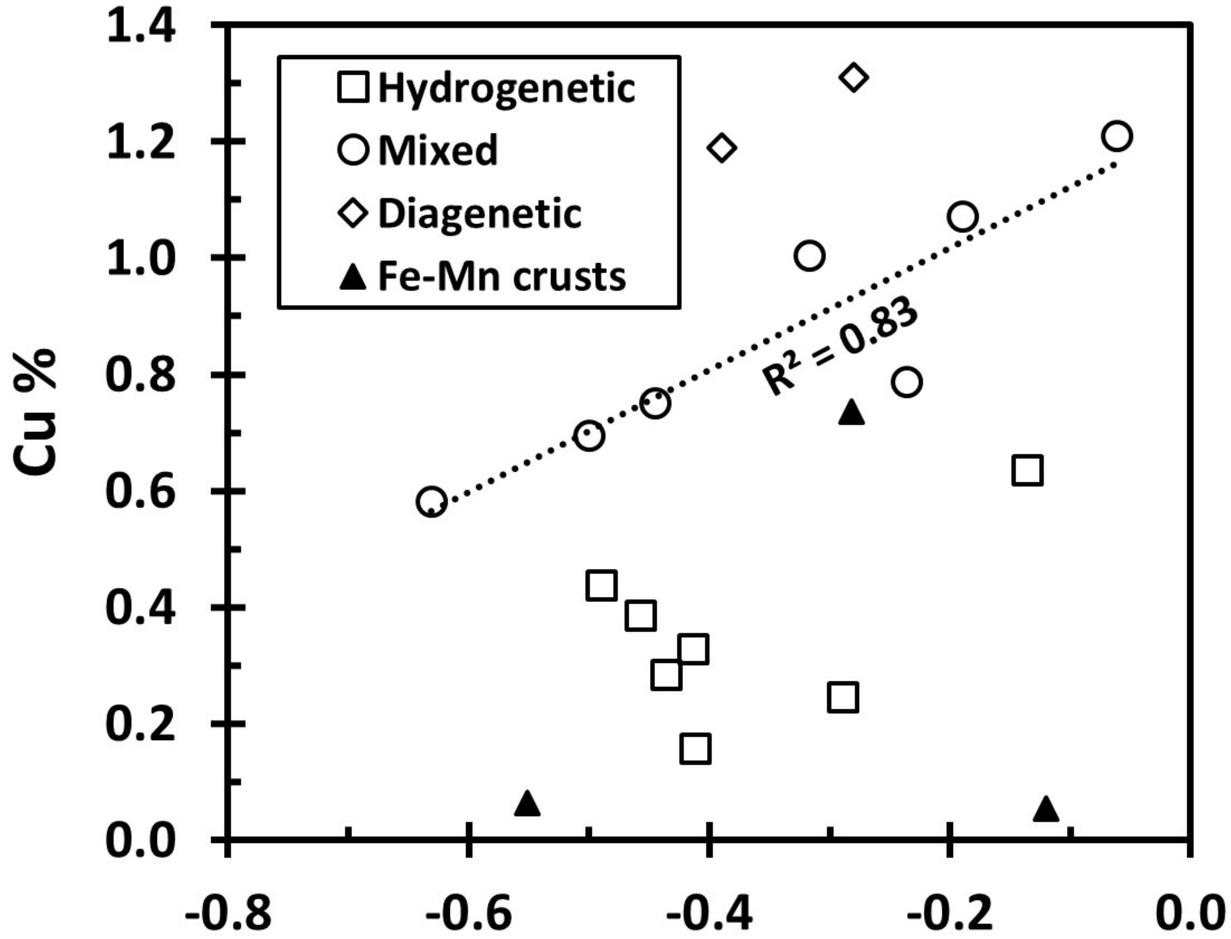

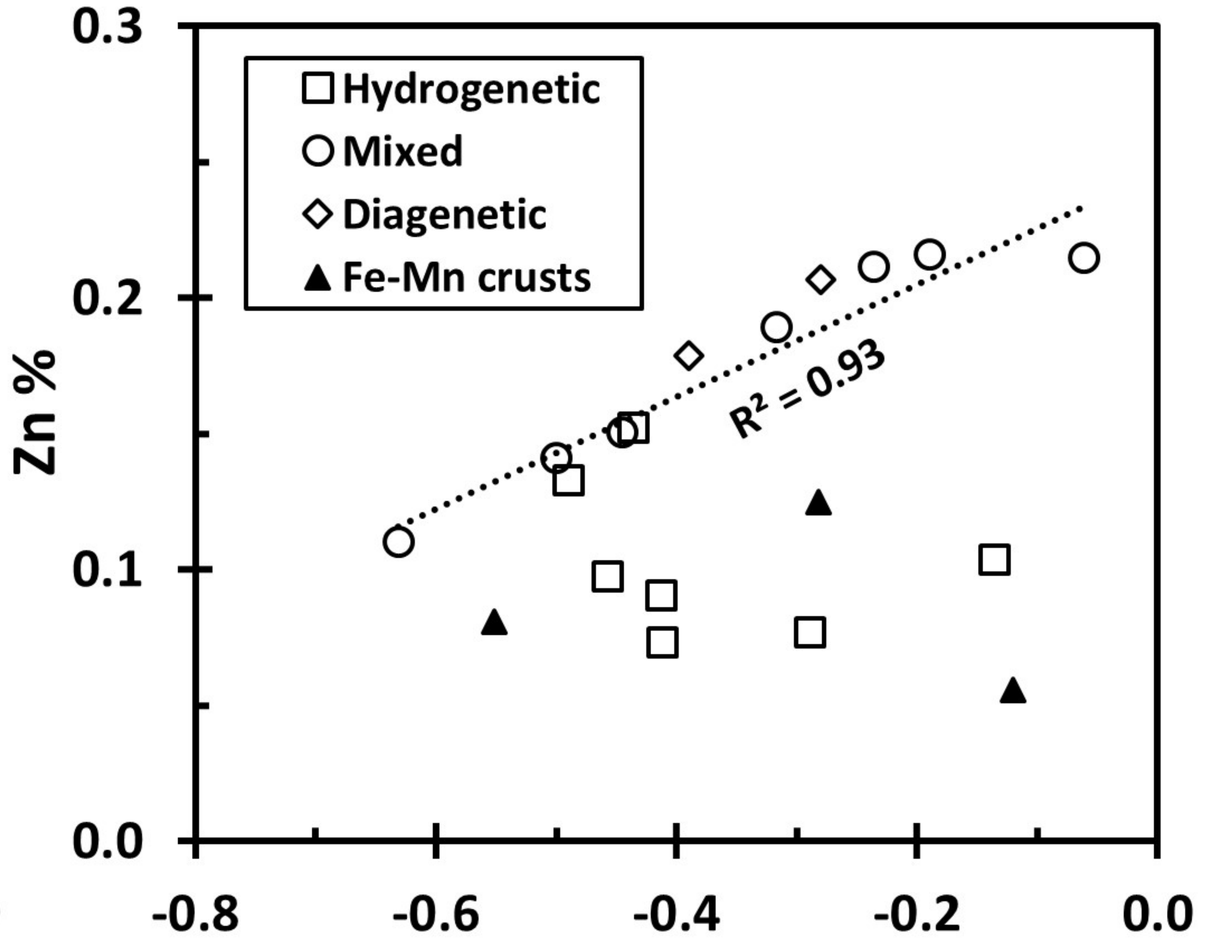

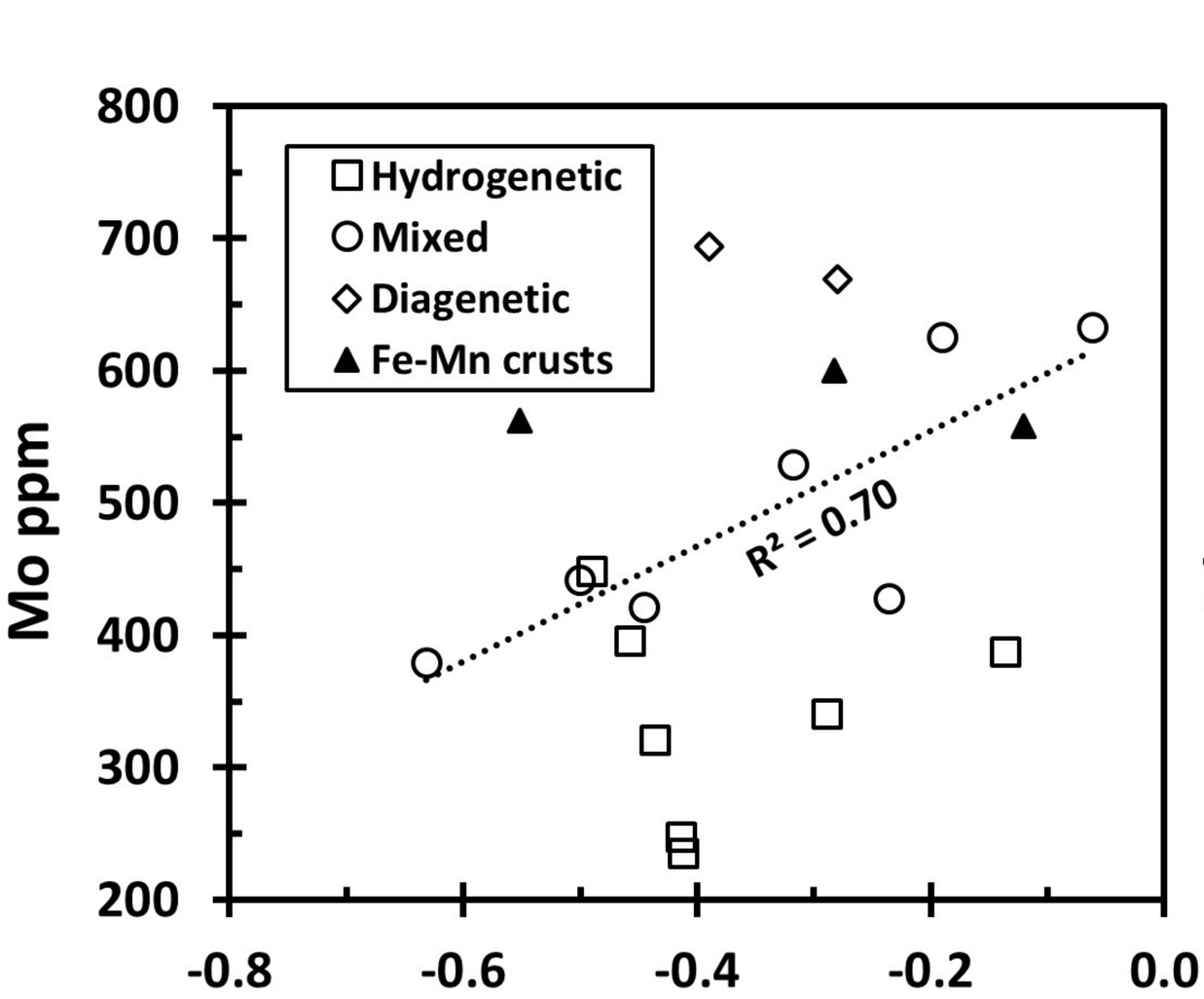

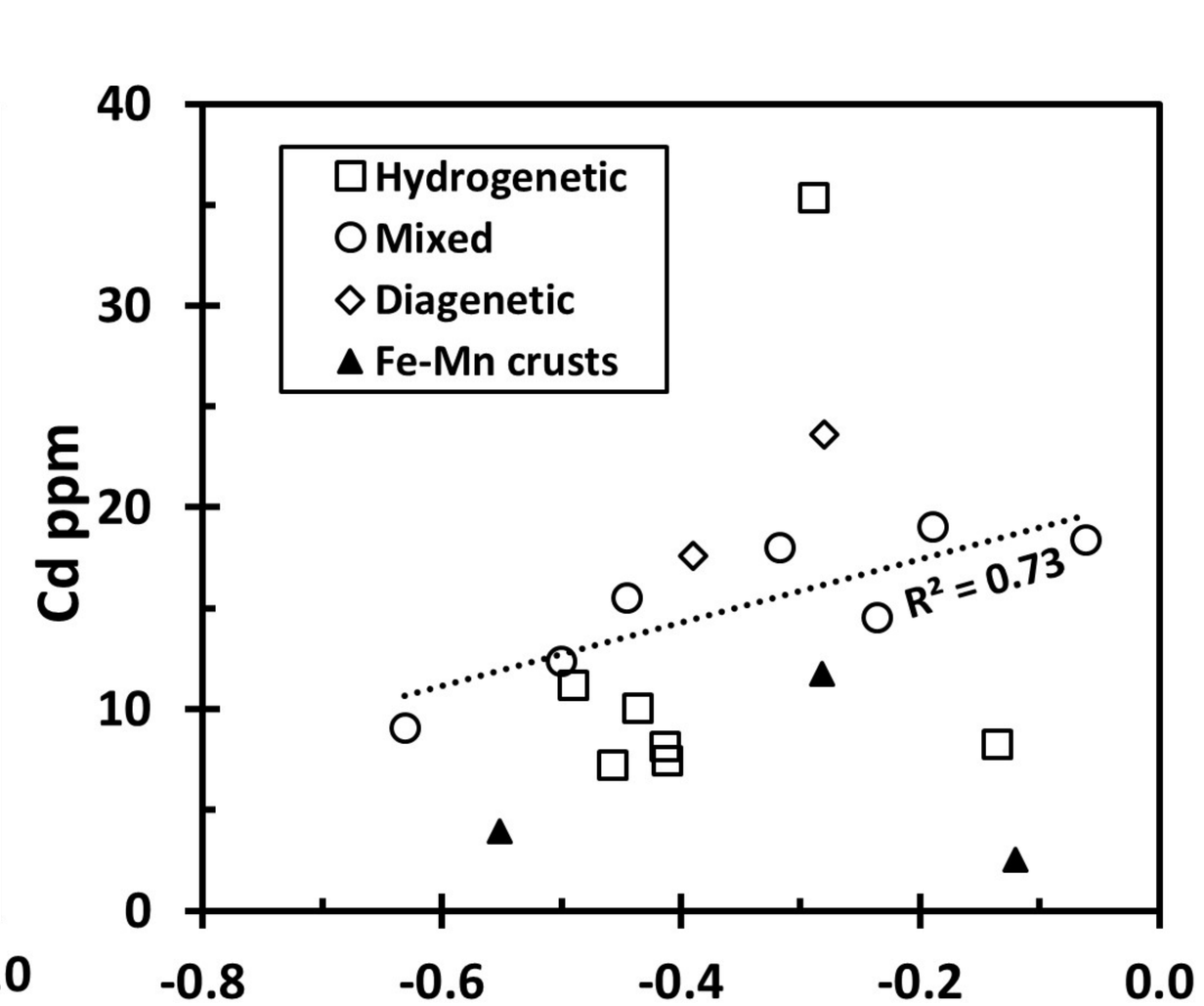

δ^{56}Fe ‰ IRMM-014

Figure.

Fe %

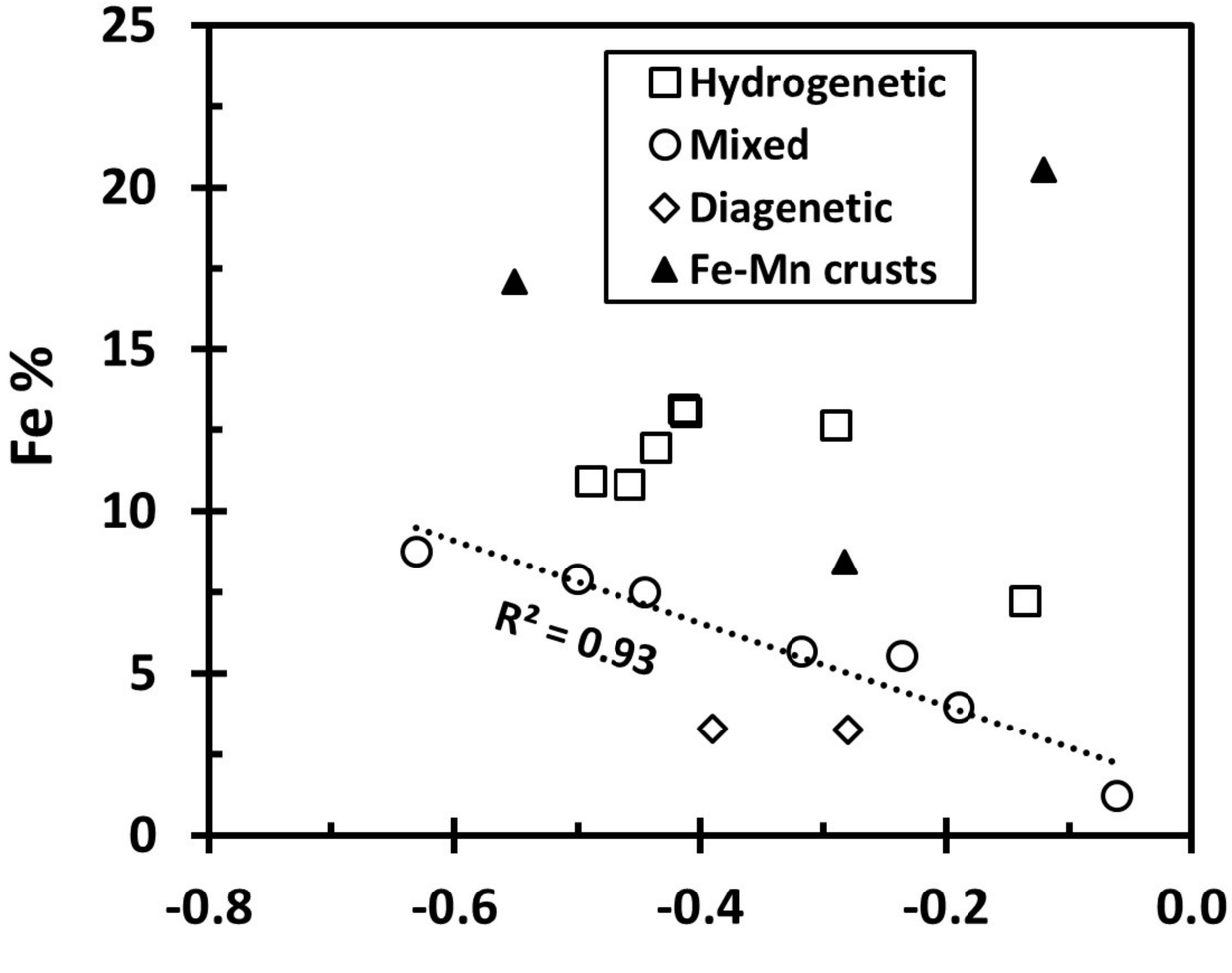

Be ppm

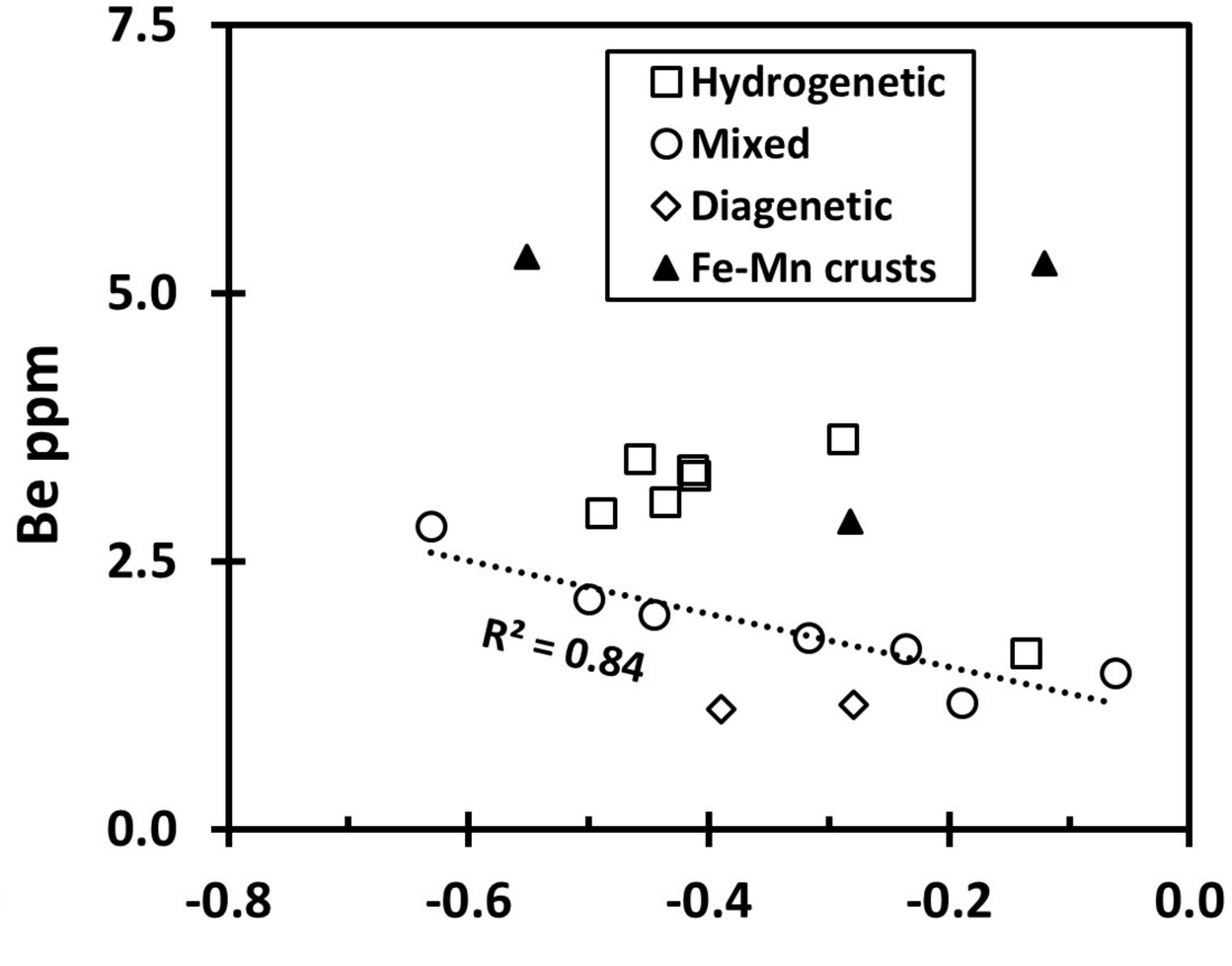

Sc ppm

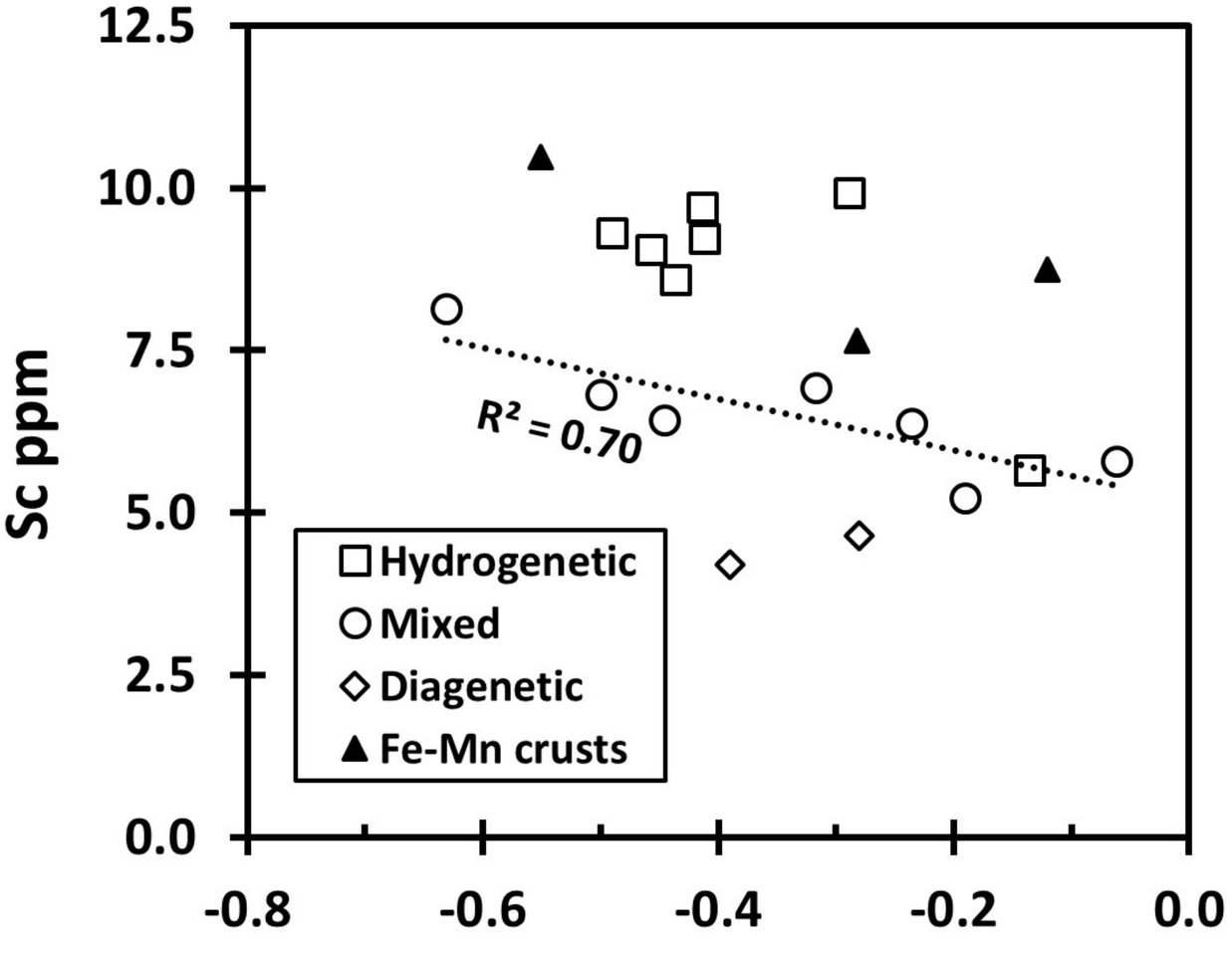

Co %

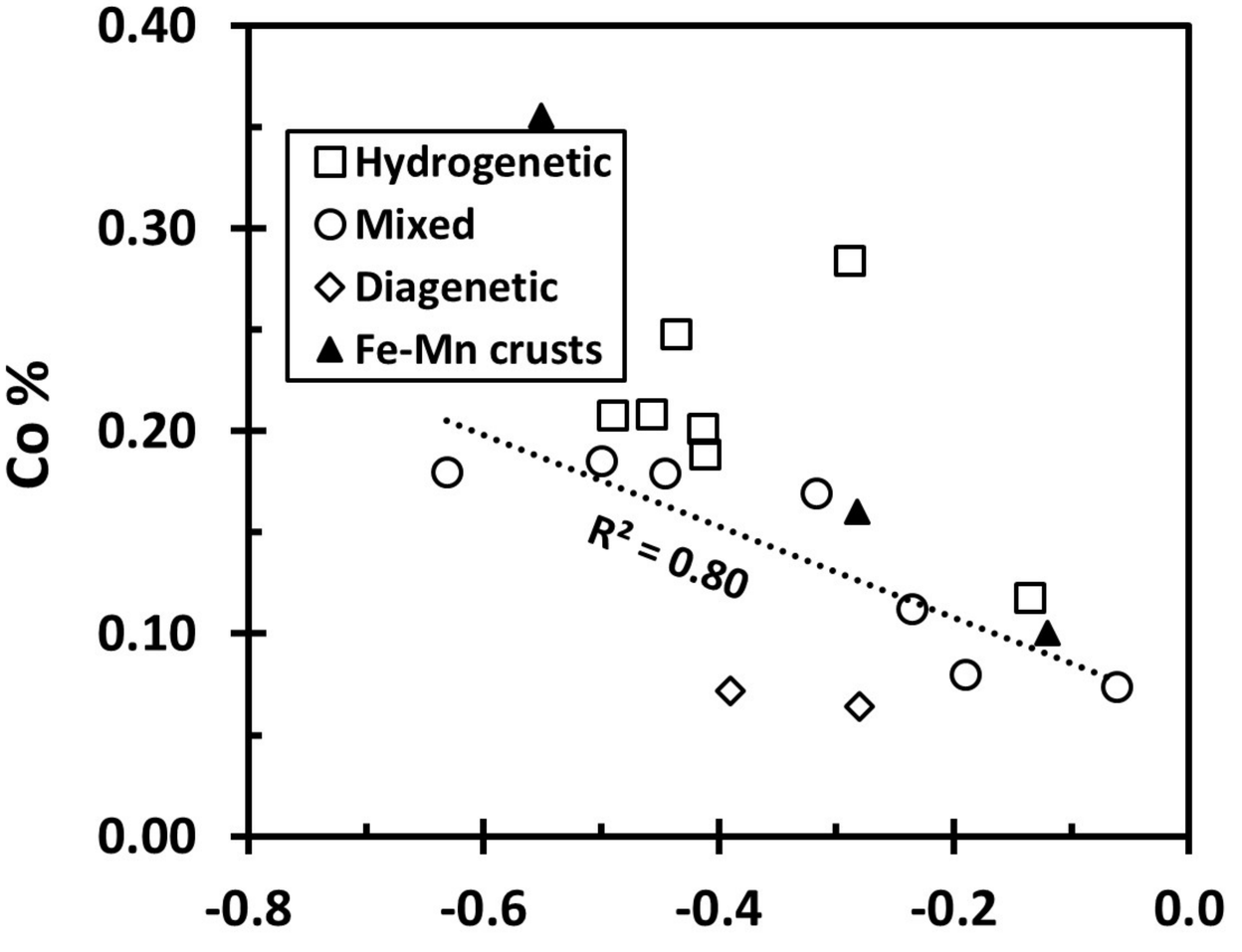

Zr ppm

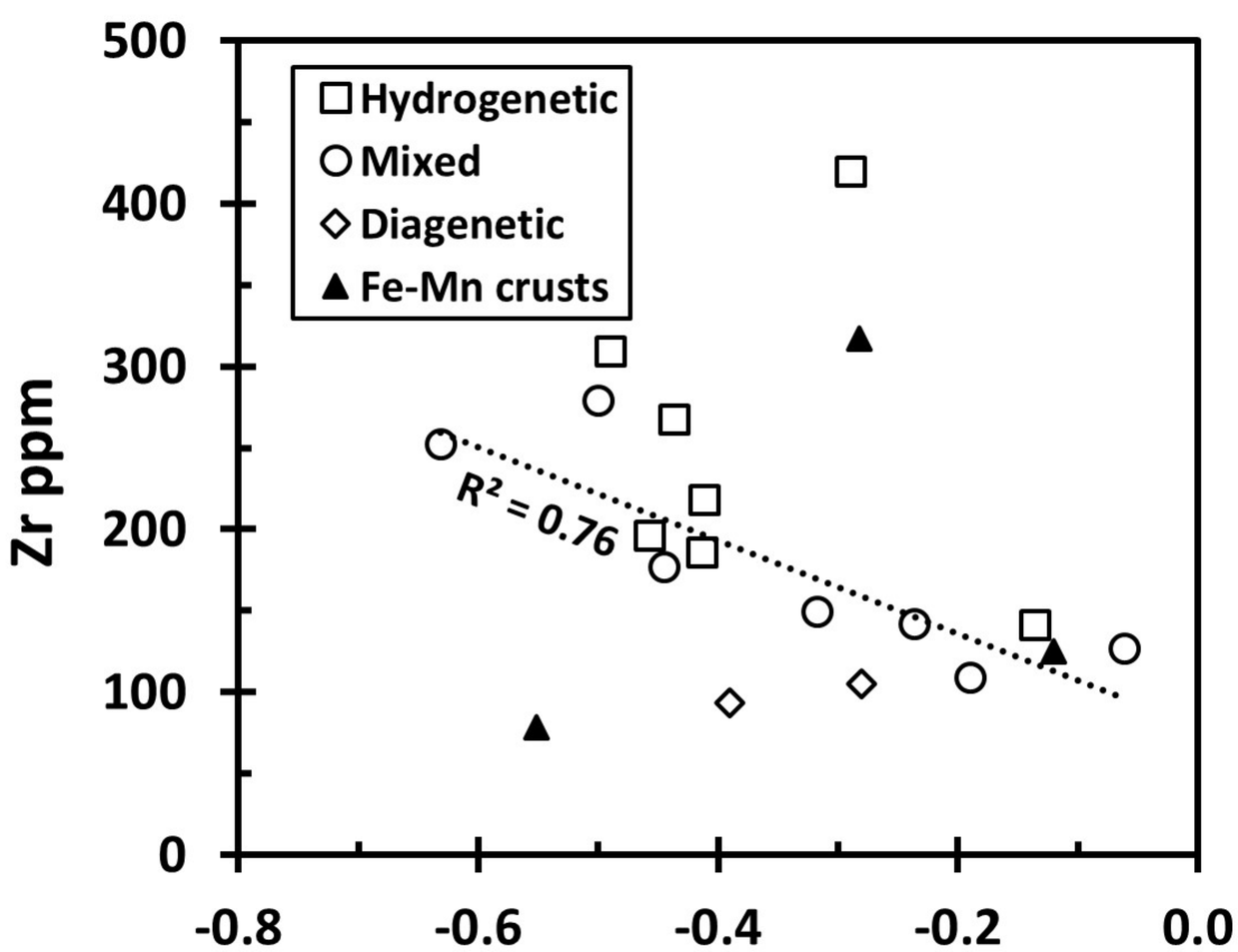

Nb ppm

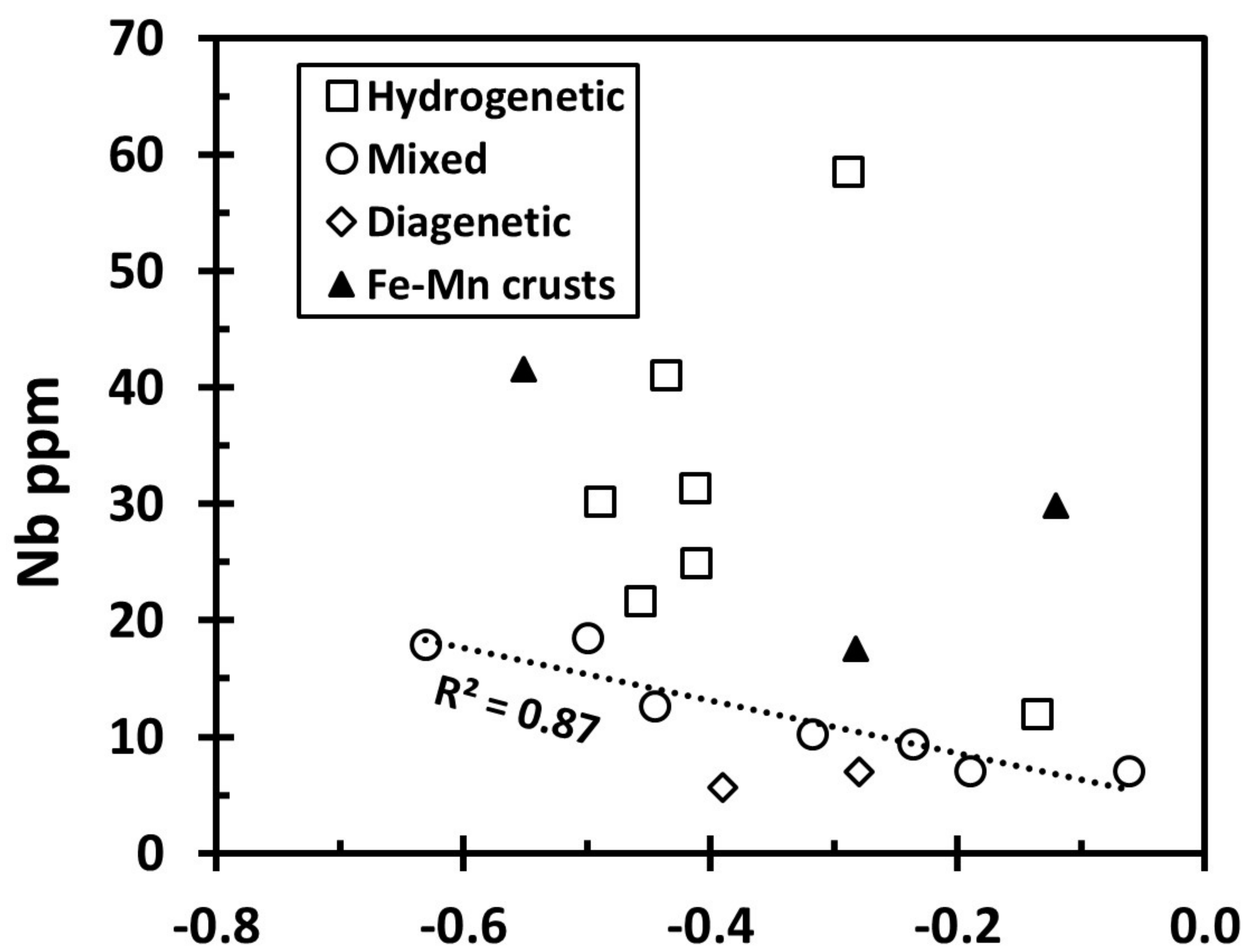

δ^{56}Fe ‰ IRMM-014

Figure.

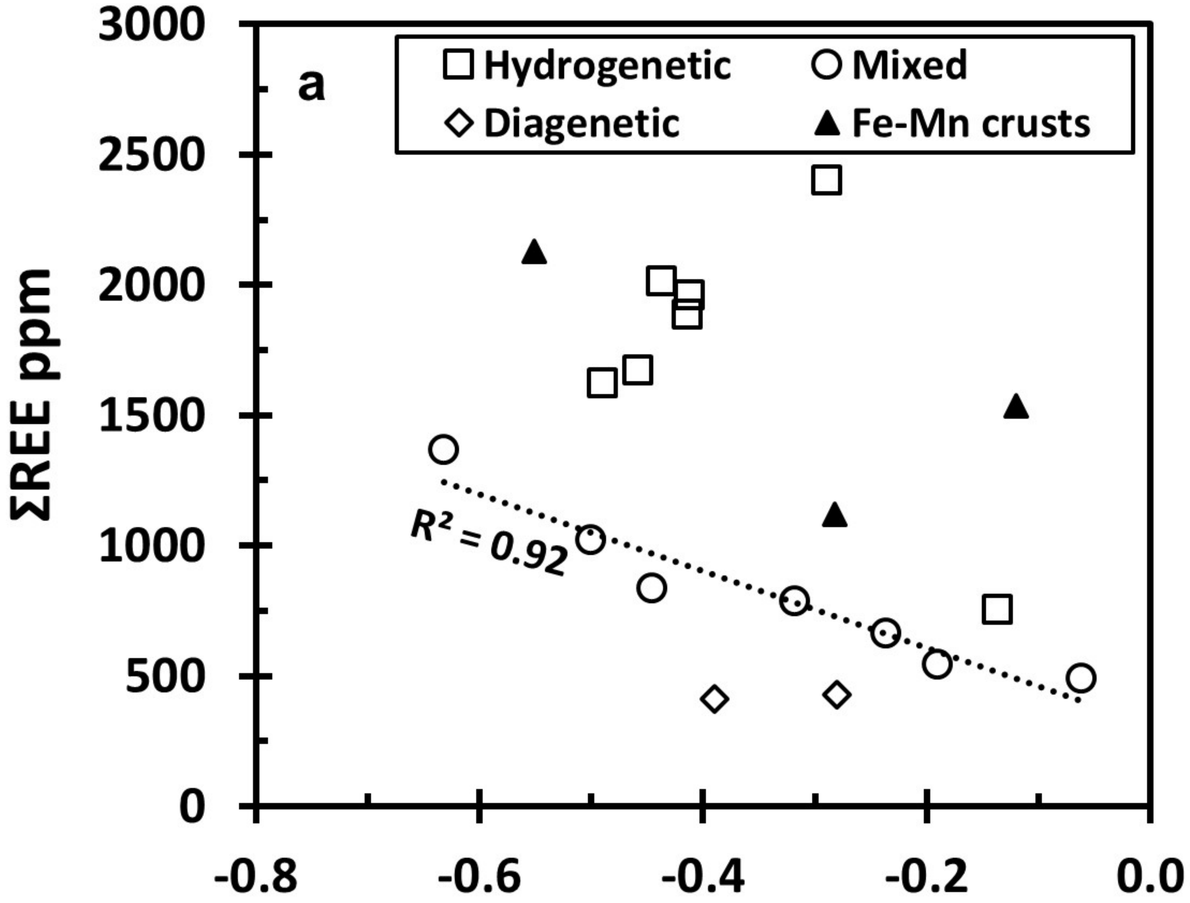
a
Hydrogenetic
Mixed
Diagenetic
Fe-Mn crusts
ΣREE ppm
3000
2500
2000
1500
1000
500
0
-0.8
-0.6
-0.4
-0.2
0.0
R² = 0.92

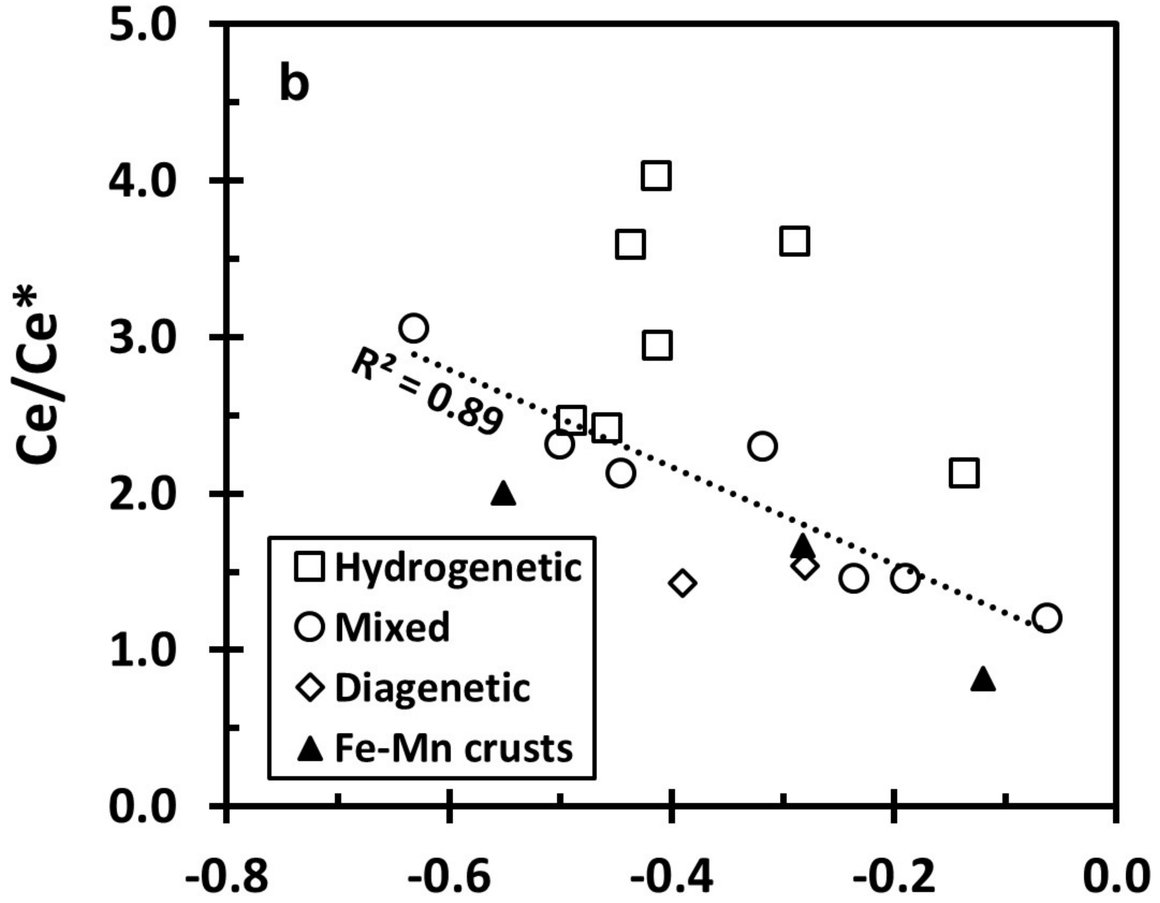
b
Ce/Ce*
5.0
4.0
3.0
2.0
1.0
0.0
-0.8
-0.6
-0.4
-0.2
0.0
R² = 0.89
Hydrogenetic
Mixed
Diagenetic
Fe-Mn crusts

Figure.

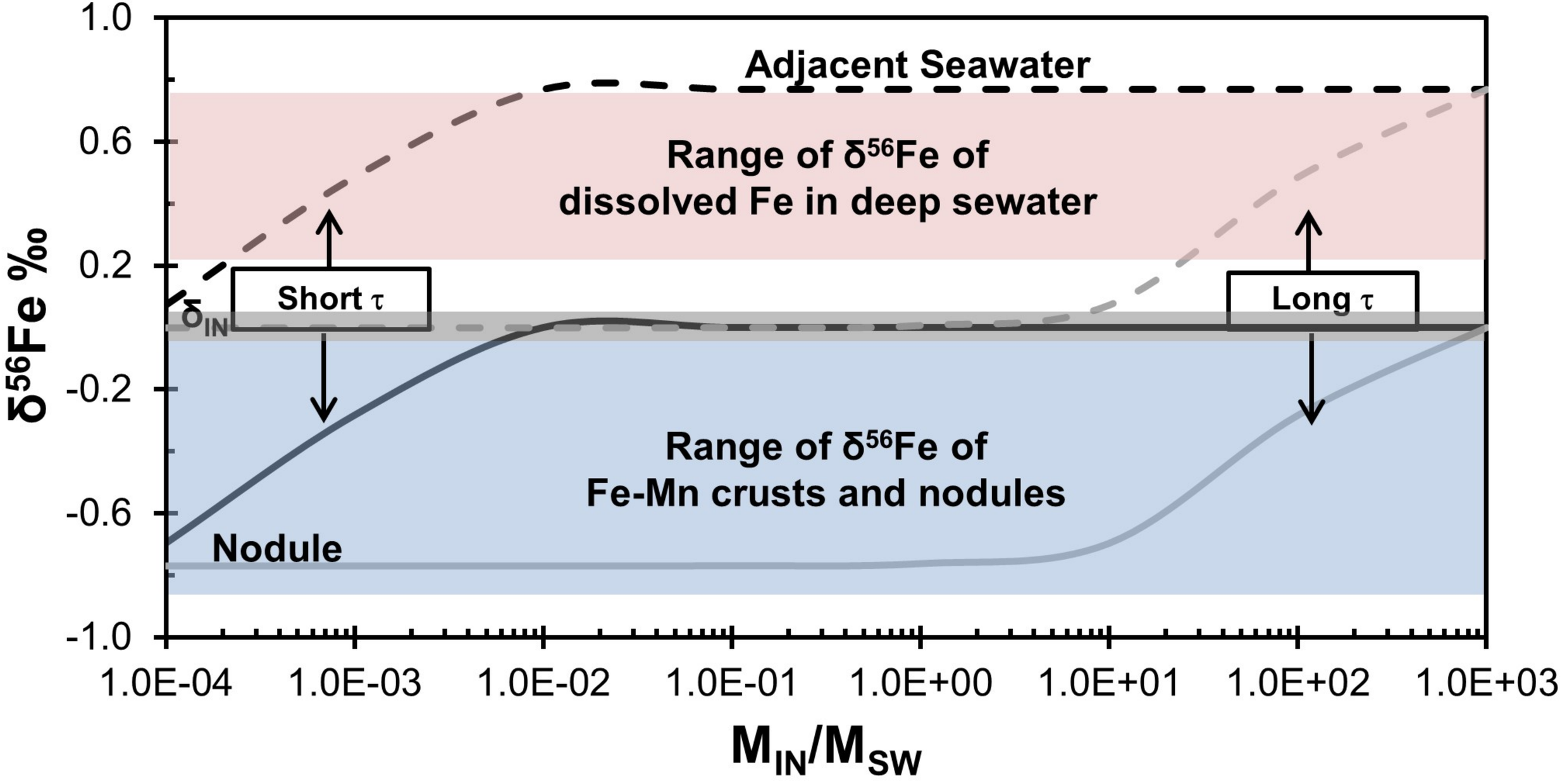
1.0
0.6
0.2
-0.2
-0.6
-1.0
δ56Fe ‰
Adjacent Seawater
Range of δ56Fe of
dissolved Fe in deep sewater
Short τ
Long τ
δIN
Range of δ56Fe of
Fe-Mn crusts and nodules
Nodule
1.0E-04
1.0E-03
1.0E-02
1.0E-01
1.0E+00
1.0E+01
1.0E+02
1.0E+03
MIN/MSW

Figure.

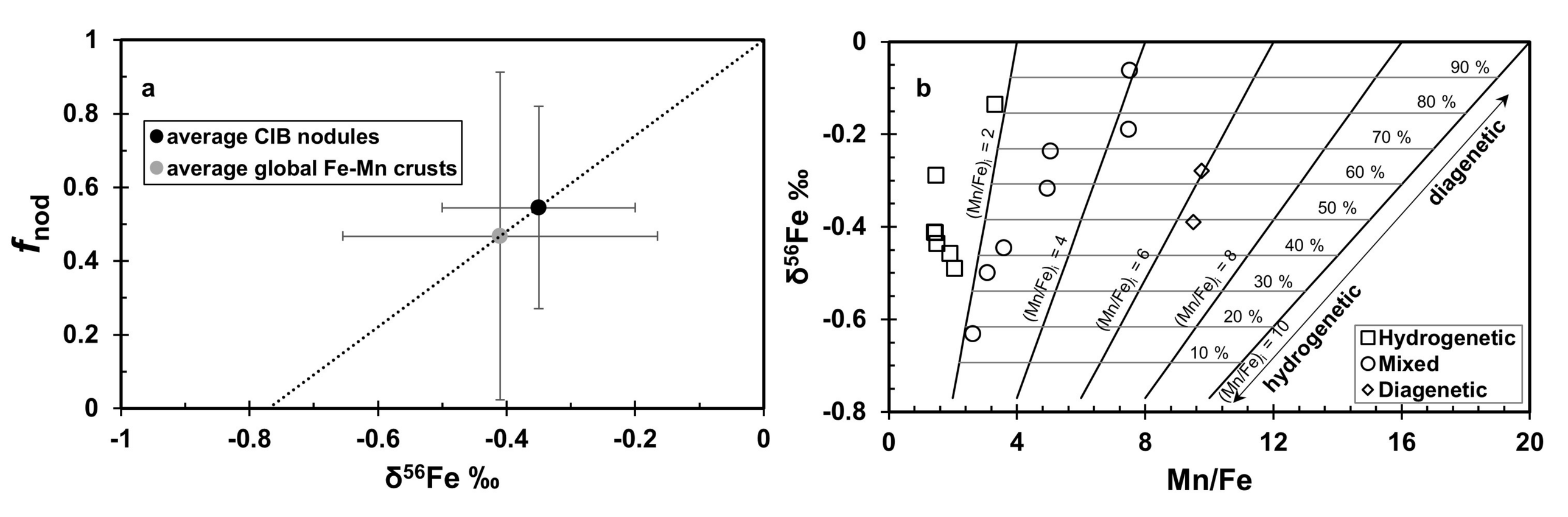
a
average CIB nodules
average global Fe-Mn crusts
f_{nod}
δ^{56}Fe ‰
b
δ^{56}Fe ‰
Mn/Fe
$(Mn/Fe)_i$ = 2
$(Mn/Fe)_i$ = 4
$(Mn/Fe)_i$ = 6
$(Mn/Fe)_i$ = 8
$(Mn/Fe)_i$ = 10
90 %
80 %
70 %
60 %
50 %
40 %
30 %
20 %
10 %
diagenetic
hydrogenetic
Hydrogenetic
Mixed
Diagenetic

Table 1 Fe isotope (δ^{56}Fe, and δ^{57}Fe ‰ IRMM-014), major and trace element data of the CIB M

	Hydrogenetic nodules					
	F-1-13-TLS	**F-3-155-TLS**	**S-3-191-TLS**	**S-3-203-TLS**	**S-4-227-TLS**	**S-4-229-TLS**
δ^{56}Fe ‰	−0.41±0.07[a]	−0.14±0.07	−0.49±0.04	−0.46±0.05	−0.44±0.07	−0.41±0.05
δ^{57}Fe ‰	−0.62[b]	−0.30	−0.76±0.15	−0.66	−0.57	−0.71
Fe %	13.02	7.19	10.89	10.78	11.93	13.12
Mn %	18.52	23.86	22.37	20.66	17.98	19.21
Mg %	1.32	2.12	1.59	1.61	1.67	1.91
Na %	1.88	1.87	1.62	2.01	0	2.7
K %	0.38	0.44	0.47	0.46	0.31	0.49
Mn/Fe	1.42	3.32	2.05	1.92	1.51	1.46
ppm						
Li	10.05	32.11	82.42	30.23	41.07	51.51
Be	3.3	1.6	2.9	3.4	3	3.3
Sc	9.2	5.6	9.3	9	8.6	9.7
Cr	4.4	4.7	3.7	3.9	10.2	3.9
Co	1882	1175	2076	2077	2475	2010
Ni	4685	11040	7866	7885	7757	8088
Cu	1567	6344	4366	3848	2817	3269
Zn	730.9	1034	1327	970	1521	900.7
Ga	8.9	12.1	12.9	10.5	12.7	13.1
Rb	6.2	9.8	8.6	9.6	6.6	10
Sr	986.4	580.6	942.5	1069	915.5	729.6
Y	106.7	53.5	88.4	107.9	90.5	76.6
Zr	217.3	140.5	308.6	195.8	267.2	185.4
Nb	24.9	11.9	30.2	21.6	41	31.3
Mo	234.5	386.6	448	394.9	320.5	247
Cd	7.4	8.2	11.1	7.2	10	8.1
Sn	1.3	0.8	1	1.1	1	0.9
Sb	12.3	24.8	22.4	21.7	23.2	23.6
Cs	0.2	0.4	0.1	0	0.3	0.2
Ba	946.3	937.4	1246	967.4	1241	1020
La	190.6	83.7	175	181.5	170.6	149.5
Ce	1296	434.1	1008	1028	1419	1381
Pr	53.6	26.2	50.6	52.6	48.5	41.5
Nd	208.2	104.8	199.6	202.7	190.6	160.5
Sm	50.2	26.3	48	48.7	45	36.3
Eu	11.9	6.1	11.1	11.6	10.5	8.6
Gd	52.8	26	47.4	50.6	49	41.1
Tb	7.9	4	7	7.7	6.8	5.7
Dy	39.3	19.3	34.1	38.2	33.2	28.1
Ho	7.8	3.9	6.5	7.9	6.5	5.4
Er	19.2	9.6	15.7	19.6	16.1	13.1
Tm	2.8	1.4	2.4	2.9	2.4	1.9
Yb	18.6	9.3	14.8	18.8	14.9	12.5
Lu	2.4	1.2	1.9	2.4	2	1.7
Hf	4.3	3.9	8.8	3.9	8.2	5.6

Ta	0.4	0.4	0.9	0.4	0.8	0.6
Tl	106.7	107.8	121.1	173.4	98.9	106.5
Pb	1630	880.2	1573	1685	1905	1555
Bi	31.6	17.1	26.7	34.4	28.3	26.5
Th	113	54.3	90	68.2	114.6	119
U	7.3	3.8	6.3	8.2	6.8	5.4

(a) The 1σ errors on δ^{56}Fe are the external errors obtained on IRMM-014 analyzed during the stud

(b) The 1σ errors on δ^{57}Fe are of the order of ±0.1 ‰.

Mn nodules and Fe-Mn crusts

	Mixed nodules					
S-7-328-TLS	S-211-TLS	S-3-144-TLS	S-3-180-TLS	S-3-201-TLS	S-4-225-TLS	SK-11-93-TLS
−0.29±0.07	−0.63±0.02	−0.24±0.05	−0.45±0.07	−0.19±0.05	−0.32±0.05	−0.50±0.03
−0.50	−0.87	−0.41	−0.62	−0.24±0.15	−0.71	−0.78±0.09
12.6	8.75	5.52	7.46	3.92	5.65	7.89
18.62	22.89	27.83	26.74	29.33	27.97	24.22
1.39	1.89	2	1.99	1.77	2.12	1.81
2.6	1.85	2.35	2.18	3.26	2.29	1.69
0.34	0.61	0.63	0.56	0.55	0.87	0.35
1.48	2.62	5.04	3.58	7.49	4.95	3.07
27.43	62.5	116.3	98	228.8	168	88.2
3.6	2.8	1.7	2	1.2	1.8	2.1
9.9	8.1	6.4	6.4	5.2	6.9	6.8
3.6	3.5	3.7	4.5	3.9	4.1	2.9
2838	1794	1118	1790	791.8	1688	1849
5690	9043	14720	10960	11120	14540	12040
2447	5805	7853	7484	10710	10030	6936
765.7	1099	2112	1501	2159	1888	1408
11.3	12	12.7	13.1	11.1	12.9	13.7
8.7	10.9	10	8.6	8.7	12.9	8.5
1055	805.7	601.3	607.8	592.9	619.4	662.5
107.8	80.2	56.4	55.2	51.9	57.7	64.6
419	251.6	141.2	176.2	108.7	148.9	278.3
58.5	17.9	9.3	12.6	7	10.2	18.4
340	378.5	427.2	420.6	624.6	528.3	441.1
35.3	9.1	14.5	15.5	19	18	12.4
0.9	1.1	0.9	0.9	1	1	1
15.9	29.4	43.6	33	58.2	51.3	32.8
0.3	0.2	0.1	0.1	0.2	0.2	0.1
1161	816.8	878.1	1109	827.8	979.4	1110
207.7	128.8	86.2	89.6	72.9	80.6	103
1701	914.3	314.1	478.3	259.9	460.8	601.3
56.6	36.8	28.5	29.8	23.1	26.4	34.7
218.1	141.8	116	118.5	92.4	107.3	139.3
51.8	33.1	29.7	29.8	23.4	27.4	35.9
12.2	8	7.2	7.1	5.6	6.6	8.5
56.3	36.3	28	29.3	22.5	27.1	34.2
7.9	5.5	4.5	4.5	3.6	4.2	5.3
39.4	27.2	21.8	21.1	17.6	20.6	25.7
7.7	5.5	4.2	4.1	3.7	4.1	4.9
19.1	13.7	10.5	10.2	9	10.2	12.1
2.9	2.1	1.6	1.5	1.4	1.5	1.8
18.7	13.6	10.1	10.1	8.6	10	11.9
2.5	1.8	1.3	1.3	1.1	1.3	1.5
11.4	5.5	3.3	4.2	2.3	3.7	7

1.1	0.5	0.3	0.4	0.2	0.4	0.7
113.8	178.4	183.3	117.7	241.4	190.7	122.7
2248	1317	799.5	917.2	766.8	858.7	991
35.2	31.1	13.8	11.4	12.4	12	14.8
122.7	55.6	44.6	51.7	21.3	39.8	70
8.1	6.3	3.7	3.7	5.4	4.2	4.2

y.

	Diagenetic nodules		Fe-Mn crusts		
R-171-TLS	S-4-260-TLS	SK-8-56-TLS	AND	CIB	SKC
−0.06±0.02	-0.39±0.08	-0.28±0.04	-0.55±0.04	-0.12±0.04	-0.28±0.04
−0.04	-0.55±0.21	-0.56±0.20	-0.95	-0.11	-0.48
4.14	3.29	3.23	17.06	20.53	8.41
31.1	31.27	31.6	17.7	14.22	25.69
1.92	1.78	2.11	1.33	1.12	1.86
2.95	3.4	2.42	1.66	1.56	2.77
0.6	0.51	0.59	0.33	0.3	0.63
7.52	9.5	9.77	1.04	0.69	3.05
143	213.5	278.1	1	0.6	65
1.4	1.1	1.2	5.3	5.3	2.9
5.8	4.2	4.6	10.5	8.7	7.6
6.4	3	3.2	2.9	2.6	3.2
736.2	718.6	640.9	3554	1003	1601
16250	12930	13000	2658	1438	11920
12090	11900	13100	628.4	544.2	7363
2144	1787	2065	807.4	554.5	1247
15.1	11.9	13.8	11.3	10.5	14.2
11.7	7.3	11.9	4.5	3	10
563.8	449.4	509.1	1,554.00	1,669.00	824.1
46.2	36.2	37.2	200.5	190.4	84.4
126.3	93.4	104.7	78.2	124.7	316.9
7	5.6	7	41.6	29.8	17.5
632.5	693.5	669.4	562.5	557.7	600.1
18.3	17.6	23.6	4	2.5	11.7
2.7	1	1.2	0.7	0.7	0.8
60.7	64.1	65.8	45.2	48.7	35.8
0.3	0.2	0.1	-0.2	-0.1	0
984.8	781.4	950.9	1,295.00	1,219.00	1,194.00
70	53.1	54.7	310	336.7	143.8
208.7	192.3	209.3	1,214.00	558.8	580.8
22.8	18.1	17.9	62.4	72.9	44.5
91.4	73	72.3	253.4	287.9	175.2
23.5	18.7	18.5	53	59.4	42.7
5.8	4.5	4.4	13.5	14.7	10.3
22.1	17.4	17.7	66.7	65.3	41.3
3.5	2.8	2.9	10.1	10.1	6.6
17.3	14.2	14	55.8	54.2	32.7
3.5	2.8	2.7	12.6	11.5	6.4
8.6	7	6.9	33.6	29.4	16.1
1.3	1.1	1	5.2	4.2	2.5
8.7	6.8	6.8	33.3	27.1	16
1.1	0.9	0.9	4.4	3.6	2.1
2.4	1.9	2.5	1.3	1.8	6.2

0.2	0.2	0.2	0.1	0.2	0.6
210.1	195.7	254	128.3	39.7	147.8
685.9	524.7	620.9	1,951.00	1,082.00	1,196.00
11.3	9	9.1	44	8.3	18
25.6	21	21	23.8	23.9	60.3
3.9	4.3	4.6	13.9	12.7	5.9